

# Accepted Article

## Observational evidence of ventilation hotspots in the Southern Ocean

Lilian A. Dove<sup>1</sup>, Andrew F. Thompson<sup>1</sup>, Dhruv Balwada<sup>2</sup>, Alison R. Gray<sup>2</sup>

<sup>1</sup>Department of Environmental Science and Engineering, Division of Geological and Planetary Sciences,  
California Institute of Technology, Pasadena, California, USA  
<sup>2</sup>School of Oceanography, University of Washington, Seattle, Washington, USA

### Key Points:

- Observations with high spatial and temporal resolution were collected from two ocean gliders following a Biogeochemical-Argo float.
- Physical and biogeochemical tracer variance is enhanced within a standing meander of the Antarctic Circumpolar Current.
- The standing meander shows evidence of heightened exchange of water properties between the ocean surface boundary layer and the interior.

---

Corresponding author: Lilian Dove, dove@caltech.edu

This article has been accepted for publication and undergone full peer review but has not been through the copyediting, typesetting, pagination and proofreading process, which may lead to differences between this version and the Version of Record. Please cite this article as doi: 10.1029/2021JC017178.

This article is protected by copyright. All rights reserved.

**Abstract**

Standing meanders are a key component of the Antarctic Circumpolar Current (ACC) circulation system, and numerical studies have shown that these features may locally enhance subduction, upwelling, as well as lateral and vertical tracer transport. Yet, observational data from these regions remain sparse. Here we present results based on measurements made by a group of autonomous platforms sampling an ACC standing meander formed due to the interaction of the Polar Front with the Southwest Indian Ridge. Two Seagliders were deployed alongside a Biogeochemical-Argo float that was advected through the standing meander. In the high eddy kinetic energy region of the standing meander, the glider observations reveal enhanced submesoscale frontal gradients as well as heightened tracer variability at depth, as compared to the more quiescent region further downstream. Vertical gradients in spicke and apparent oxygen utilization are reduced in the standing meander despite similarities in the large-scale vertical stratification, suggesting greater ventilation of the surface ocean. These observations are consistent with numerical studies that highlight standing meanders as hotspots for ventilation and subduction due to enhanced mesoscale stirring and submesoscale vertical velocities. Our results emphasize the need to account for spatial heterogeneity in processes influencing air-sea exchange, carbon export, and biogeochemical cycling in the Southern Ocean.

**Plain Language Summary**

The Southern Ocean plays a vital role in taking up carbon dioxide and heat from the Earth's atmosphere. Yet, historically, this region has suffered from a lack of direct observations, making it difficult to quantify rates of exchange. In regions where the strongest currents of the Southern Ocean interact with underwater topography, turbulence and mixing may be locally enhanced. Data collected from two different types of robotic vehicles, including steerable ocean gliders, were used to study one of these mixing "hotspots." The instrumented platforms provided expanded data as compared to typical Southern Ocean observational techniques. The results show that these turbulent regions allow water properties, such as temperature and oxygen, to mix vigorously. In particular, at these hotspots the exchange of waters between the ocean surface and interior increases. It is important to document the magnitude and regional patterns of this exchange because only surface waters interact with the atmosphere to take up or release carbon and heat, while interior waters store these properties for centuries or longer. Numerical models of the ocean have indicated that these turbulent regions of the Southern Ocean are particularly influential, and we provide some of the first observational evidence confirming these hotspots importance.

**1 Introduction**

The Southern Ocean exerts a strong control on the global climate as the primary site of both deep water ventilation at the ocean surface and subduction of newly-formed intermediate water masses (Marshall & Speer, 2012). Tilted density surfaces spanning the Antarctic Circumpolar Current (ACC) expose a range of density classes at the ocean surface, causing the Southern Ocean to be a key site for the uptake and sequestration of anthropogenic carbon dioxide from the atmosphere (Frölicher et al., 2015; Gruber et al., 2019). Observations in the Southern Ocean have historically been both spatially and temporally sparse, contributing to disagreements between carbon uptake estimates in models and observations (Gruber et al., 2019) and limiting attribution to specific processes that explain these discrepancies. The deployment of Biogeochemical-Argo (BGC-Argo) floats as part of the Southern Ocean Carbon and Climate Observations and Modeling (SOCCOM) project, which began in 2014, has started to fill the gap in observations of biogeochemical tracers, especially in winter months (Riser et al., 2016; Johnson et al., 2017; Gray et al., 2018). The typical float sampling strategy of repeat profiling

every ten days maximizes the temporal and spatial coverage of the resulting dataset, at the cost of aliasing mesoscale and submesoscale dynamics that can have a leading order impact on larger-scale Southern Ocean properties (Rintoul, 2018). Due to the lack of high-frequency subsurface observations, the impact of mesoscale and submesoscale processes on modulating biogeochemical tracer distributions in the Southern Ocean remains largely unresolved.

Export production, the flux of net primary production across the base of the ocean's euphotic zone, is a critical step for the sequestration of carbon from the atmosphere into the deep ocean (Buesseler & Boyd, 2009; Sallée et al., 2012; Levy et al., 2013). Our appreciation of the complexity of the organic carbon pump has expanded in recent years (Boyd et al., 2019), making it clear that the vertical carbon flux associated with gravitational sinking alone is insufficient to close the carbon budget (Boyd et al., 2019; Levy et al., 2013; Schlitzer, 2002). Ecological processes (*e.g.* predator migration) and physical processes have both been highlighted as potential mechanisms for enhancing carbon export fluxes (Lévy et al., 2012; Omand et al., 2015; Lévy et al., 2018). Physical processes that contribute to non-gravitational carbon export are associated both with modulation of mixed layer depths (MLDs) and with direct transport by vertical motions across the base of the mixed layer. The MLD changes in response to wind and buoyancy forcing, the latter caused by surface heating, freshwater fluxes, or sea ice melt that act dominantly at seasonal timescales with contributions from processes occurring at higher-frequency timescales as well (Palevsky et al., 2016; Dall'Olmo et al., 2016; Bol et al., 2018). Export may also occur via subduction processes at frontal zones due to associated strong vertical velocities (Klein & Lapeyre, 2009). The three-dimensional overturning structure and energetic eddy field of the Southern Ocean preconditions this region to have a significant contribution to export from physical processes (Omand et al., 2015; Llort et al., 2018).

Assessment of the potential for physical export in the Southern Ocean must account for the multi-scale nature of the circulation. At larger scales, the ACC is comprised of a series of eastward-flowing frontal jets that are typically efficient water mass barriers (Orsi et al., 1995). These frontal flows are accompanied by strongly tilting density surfaces in thermal wind balance that allow for the adiabatic ventilation of deep waters and sustain a vigorous mesoscale eddy field (Rintoul & Naveira Garabato, 2013). A small number of standing meanders form in the ACC where these jets interact with major topographic features, including one arising from the flow of the Polar Front (PF) over the Southwest Indian Ridge (SWIR). This standing meander is the focus of this study (Figure 1). In these standing meander regions, flow-topography interactions can cause transport barriers to become "leaky" (Naveira Garabato et al., 2011) as well as enhance eddy kinetic energy (EKE) (Gille & Kelly, 1996; Witter & Chelton, 1998; Lu & Speer, 2010), vertical momentum transport (Thompson & Naveira Garabato, 2014), lateral tracer transport (MacCready & Rhines, 2001; Thompson & Sallée, 2012; Dufour et al., 2015; Roach et al., 2016), upwelling (Viglione & Thompson, 2016; Tamsitt et al., 2017), and subduction (Llort et al., 2018; Bachman & Klocker, 2020). Observational studies of the circulation in the SWIR region, *e.g.*, Pollard and Read (2001), have identified a steady, largely barotropic jet associated with the PF, which is stabilized by the ridge before "fragmenting" into multiple smaller-scale jets further downstream. This area plays a central role in the upwelling branch of the overturning circulation (Tamsitt et al., 2017).

ACC standing meanders are characterized by enhanced EKE and strain rates due to persistent conditions favorable for baroclinic and barotropic instabilities (Lu et al., 2016; Youngs et al., 2017). The imprint of coherent eddies on tracer structure, *e.g.* surface chlorophyll, occurs over horizontal scales of  $O(10\text{-}100\text{ km})$ . These eddies typically have a vertical extent of  $O(2000\text{ m})$  and stir tracers below the mixed layer in the interior (Balwada et al., 2016, 2020). Near the surface, mesoscale eddies usually have an inlay of strong submesoscale  $O(1\text{-}10\text{ km}, 1\text{ hour}\text{-}10\text{ days})$  currents, which are often visi-

ble as cusps and filaments in surface tracers. These smaller scale motions are energized by the production of surface buoyancy gradients through mesoscale frontogenesis (Klein & Lapeyre, 2009; Adams et al., 2017) and by the formation of submesoscale eddies through mixed layer baroclinic instabilities (Boccaletti et al., 2007) or through wind-front interactions (Thomas et al., 2008). Submesoscale currents are generally associated with elevated vertical velocities and restratification tendencies in the mixed layer (Su et al., 2018). Strong vertical velocities may penetrate up to a few 100 m below the base of mixed layer (Siegelman et al., 2020), playing an important role in transporting material across the base of the mixed layer and connecting the surface ocean to the mesoscale-dominated interior.

Both observational and modeling studies have confirmed that the Southern Ocean has an active submesoscale flow field (Rosso et al., 2014; Adams et al., 2017; Bachman et al., 2017; Viglione et al., 2018; du Plessis et al., 2017, 2019), although the degree to which submesoscale motions are effective at enabling surface-interior exchange has been limited to modeling studies (Brannigan, 2016; Mahadevan, 2016; Balwada et al., 2018; Uchida et al., 2019). In some regions, strong upper-ocean vertical stratification, often induced by sea-ice melt in the marginal ice zone, may limit the vertical extent of submesoscale motions (Swart et al., 2020). However, observations in a region of vigorous EKE and mesoscale strain further to the north have been used to infer enhanced vertical velocities well below the ocean surface (Siegelman et al., 2019). Constraining the impact of submesoscale dynamics on vertical tracer exchange from observations requires high spatial- and temporal-resolution measurements that are challenging to acquire, particularly in regions with a strong mean flow. Inhomogeneity in submesoscale variability is a key feature of the Southern Ocean that appears to be strongly shaped by interactions with topography (Rosso et al., 2015; Viglione et al., 2018).

Tracer variability arising from mesoscale is difficult to distinguish from that caused by submesoscale dynamics, and previous modeling work has demonstrated the close link between these scales. Increasing model resolution leads to the production of more small-scale features, but they remain structured around the mesoscale eddy field (Balwada et al., 2018). Mesoscale strain has also been shown to be a proxy for the magnitude of submesoscale vertical velocities (Rosso et al., 2015; Siegelman et al., 2020). The entangled nature of mesoscale and submesoscale flows, together with the three-dimensional nature of the currents, means that while fine-scale structure in tracer variability is a well-known feature of the Southern Ocean (Joyce et al., 1978; Pollard & Read, 2001), attribution of this structure to specific dynamical processes remains challenging.

The primary goal of the Southern Ocean Glider Observations of Submesoscales (SO-GOS) project was to observe the variability of physical and biogeochemical properties around a BGC-Argo float at much higher spatial and temporal resolution than the typical float sampling, through the use of two ocean gliders. Details of the autonomous platforms and their sampling capabilities are provided in Section 2, and the measurements collected by these platforms that are used to examine the influence of mesoscale and submesoscale processes on ventilation are presented in Section 3. Section 4 considers these measurements in the context of recent numerical simulations and shows that the observational evidence supports the hypothesis that ACC standing meanders are sites of enhanced Southern Ocean ventilation. We conclude in Section 5 by suggesting how these results inform sampling strategies of future Southern Ocean observing systems (Meredith et al., 2013) as well as our ability to monitor future changes to the Southern Ocean carbon sink.

## 165 2 Data and Methods

### 166 2.1 Autonomous platforms and sensors

167 The SOGOS field campaign began with the deployment of two Seagliders (SG659  
 168 and SG660) in conjunction with a SOCCOM BGC-Argo float (WMO 5906030) on May  
 169 1, 2019 at 51.49°S, 30.03°E, from the I06S GO-SHIP cruise (April-May 2019, [www.go-ship.org](http://www.go-ship.org)).  
 170 All platforms were advected downstream to the east, experiencing meridional deviations  
 171 due to flow meanders. The float and gliders sampled immediately in the lee of the SWIR,  
 172 a major topographic feature in the western Indian sector of the Southern Ocean; the ob-  
 173 servation region fell roughly between 30°E to 40°E and 50°S to 54°S (Figure 2). The glid-  
 174 ers sampled for a period of 86 days, ending their mission on July 25, 2019. SG659 and  
 175 SG660 completed 462 and 509 V-shaped profiles from the surface to 1000 m and back,  
 176 respectively, with 3-5 hours (average 4.5 hours) and 2-4 km (average 3.25 km) between  
 177 surfacings. The BGC-Argo float has continued to profile since deployment and remains  
 178 active as of the submission date of this manuscript. During the dedicated SOGOS pe-  
 179 riod, the float sampled at five-day intervals, completing 16 vertical profiles. The drift-  
 180 ing depth of the float was 1000 m, and the profile depth alternated between 2000 m and  
 181 1000 m during the five-day interval sampling.

182 The SOCCOM BGC-Argo profiling float was equipped with a suite of sensors to  
 183 collect profiles of physical and biogeochemical properties in the upper 2000 dbar. A stan-  
 184 dard conductivity-temperature-depth (CTD) sensor (SeaBird 41CP) recorded bin-averaged  
 185 salinity, temperature, and pressure at 2-m vertical resolution above 1000 m and 100-m  
 186 vertical resolution below. Dissolved oxygen concentrations were measured with an Aan-  
 187 deraa 4330 optode (Tengberg et al., 2006) at variable vertical resolution, and these data  
 188 were calibrated using float-based observations of atmospheric oxygen (Johnson et al., 2015).  
 189 The float detected chlorophyll fluorescence and optical backscatter at 700 nm with a WET  
 190 Labs FLBB (Hantjens et al., 2017). Nitrate and pH were also measured using an ultra-  
 191 violet spectrophotometer (Johnson et al., 2013) and an ion-sensitive field effect transis-  
 192 tor (Johnson et al., 2016), respectively, although those data are not used in the present  
 193 study.

194 The gliders each carried unpumped CTD (CT-Sail) sensors measuring conductiv-  
 195 ity (salinity), temperature, and pressure; an Aanderaa oxygen optode; and a WET Labs  
 196 ECO puck that measured induced fluorescence and optical backscatter. The salinity and  
 197 temperature data from the glider sensors were calibrated to deep (>600 m) values from  
 198 a ship-based profile taken during the congruous I06S GO-SHIP cruise at the deployment  
 199 site. Calibration of the gliders to the float was performed when the gliders and float were  
 200 within 10 km of each other. No sensor drifts were observed but pressure-dependent off-  
 201 sets of the temperature and salinity were used for each glider. Oxygen measurements were  
 202 collected over the full 1 km dive depth; to conserve battery power, optical measurements  
 203 were collected down to 400 m with occasional dives down to 1 km to determine a back-  
 204 ground signal. Oxygen measurements were calibrated with reference to the float when  
 205 the float and each glider were within 10 km of each other. Only deep (>600 m) waters  
 206 were used for calibration to account for surface variability and used to calculate a gain  
 207 correction for the glider oxygen, similar to the method pioneered in Johnson et al. (2015).  
 208 A pressure correction was also applied to the gliders' oxygen measurements below the  
 209 mixed layer.

210 Optical backscatter data on the gliders were measured at two wavelengths: 470 nm  
 211 and 700 nm. Raw sensor counts were calibrated using the manufacturer-supplied scale  
 212 factor and dark counts. The resulting volume scattering function includes scattering sig-  
 213 nal from pure seawater and particulate scattering (Zhang et al., 2009; Vaillancourt et  
 214 al., 2004). The scattering by seawater was calculated using a function described in Zhang  
 215 et al. (2009) and subtracted from the volume scattering function. The resulting partic-  
 216 ulate volume scattering function was converted into particulate optical backscattering

217 coefficient  $b_{bp}$  (Bol et al., 2018; Briggs et al., 2011). Finally, following Briggs et al. (2011),  
 218 the backscatter data were filtered using a seven-point minimum filter followed by a seven-  
 219 point maximum filter in order to remove spikes, which often occur in profiles of  $b_{bp}$  due  
 220 to aggregate material.

221 Glider data were objectively mapped onto a regular grid with 10-m depth resolution  
 222 along the vertical axis and 500-m distance resolution along the horizontal axis, us-  
 223 ing a Gaussian weighting function with a vertical scale of 20 m and a horizontal scale  
 224 of 5000 m. A visual comparison of the raw data to the objectively-mapped data set re-  
 225 vealed no significant biases due to this choice of resolution. The time associated with each  
 226 glider position was interpolated to the horizontal distance grid to give an along-track time  
 227 in number of days since January 1, 2019.

228 Several additional quantities were derived from the measured properties. Poten-  
 229 tial density and spice, a variable most sensitive to isopycnal thermohaline variations and  
 230 least correlated with the density field, were calculated from temperature and salinity us-  
 231 ing the Thermodynamic Equation of Seawater 2010 (McDougall & Barker, 2011). Ad-  
 232 jacency of positive (warm, salty) and negative (cold, fresh) spice anomalies can be used  
 233 to identify thermohaline intrusions. The MLD was defined by a density difference cri-  
 234 teria of  $0.05 \text{ kg m}^{-3}$  from a 10-m reference level. We follow the methods of previous work  
 235 (Thompson et al., 2016; Viglione et al., 2018) to calculate the Ertel Potential Vorticity  
 236 (PV) from the glider data, estimated here as

$$237 \quad PV \approx fN^2 - M^4f^{-1}, \quad (1)$$

237 where  $N^2 = b_z$ ,  $M^4 = b_x^2$ , and  $b = g\rho_0^{-1}(\rho_0 - \rho)$ . Here,  $\rho$  is potential density and  
 238 subscripts indicate partial derivatives and  $x$  is in the along-glider-trajectory direction.  
 239 Discussion of the assumptions and limitations associated with estimating PV from glider  
 240 data using (1) is described in detail in the aforementioned studies. From the biogeochem-  
 241 ical measurements, apparent oxygen utilization (AOU) was calculated as the difference  
 242 between the measured oxygen and the oxygen saturation value for a given salinity and  
 243 potential temperature.

## 244 2.2 Additional data sets

245 Hourly estimates of surface forcing fields for the region during the study period were  
 246 obtained from the ERA-5 atmospheric reanalysis (data DOI: <https://doi.org/10.24381/cds.bd0915c6>). Net surface heat flux was calculated as the sum of the shortwave, long-  
 247 wave, sensible and latent heat flux estimates. Surface freshwater flux was computed us-  
 248 ing the total precipitation and evaporation estimates. Surface wind stress was calculated  
 249 using the 10 m winds ( $u_{10}, v_{10}$ ) and a simple drag law;  $\tau = \rho C_d U^2$ , where  $\rho = 1.225$   
 250  $\text{kg m}^{-3}$  is the air-density,  $C_d = 0.00125$  is the drag coefficient (set constant here for sim-  
 251 plicity), and  $U^2$  is the square of the wind speed. The zonal and meridional components  
 252 of the wind stress were calculated as  $\tau_x = \tau(u_{10}U^{-1})$  and  $\tau_y = \tau(v_{10}U^{-1})$ .

253 Daily estimates of sea surface height (SSH) relative to the geoid for the time pe-  
 254 riod 2017-2020 were obtained from the L4-gridded satellite altimeter product provided  
 255 by Aviso+ (<https://www.aviso.altimetry.fr/en/data.html>), along with  $u'$  and  $v'$ ,  
 256 the zonal and meridional geostrophic velocities associated with the time-varying, anomalous  
 257 component of the SSH field. Regional EKE was calculated as  $EKE = \frac{1}{2}\sqrt{u'^2 + v'^2}$ .  
 258 The mean was computed over the period 2017-2020, although the magnitude and spa-  
 259 tial pattern of EKE did not vary significantly from year to year. SSH, represented by  
 260 absolute dynamic topography (ADT), is determined as the sum of the time-mean dy-  
 261 namic topography and time-varying sea level anomaly. ADT values at the glider and float  
 262 locations were determined using the satellite gridpoint closest to the surfacing location  
 263 of the instrument.

265 **3 Results**

266 **3.1 Regional variability**

267 We first describe the large-scale variability within the study region, with an em-  
 268 phasis on how the sampling of the autonomous platforms during the SOGOS mission fits  
 269 into that broader picture. As noted above, the circulation in this area is dominated by  
 270 the standing meander that forms through the interaction of the PF with the SWIR (Fig-  
 271 ure 1). The meridional variability of the PF immediately downstream of the SWIR (based  
 272 on satellite observations following the methods of Kim and Orsi (2014)) illustrates that  
 273 the frontal position is relatively constant upstream of the SWIR as compared to just down-  
 274 stream (Figure 1b). The downstream variability is consistent with a breakdown of the  
 275 zonal flow and the formation of mesoscale eddies. Mean EKE accordingly reaches a lo-  
 276 cal maximum within the standing meander (Figure 2a).

277 All SOGOS platforms spent most of their time sampling close to the PF in waters  
 278 collocated with SSH values of approximately -0.7 m, hereafter referred to as PF core wa-  
 279 ters (Figure 2b). Within these waters, the gliders and float captured two distinct flow  
 280 regimes. The mean EKE within the standing meander portion (between 30°E to 33°E  
 281 and 50°S to 52°S) was  $460 \text{ cm}^2 \text{ s}^{-2}$ , over an order of magnitude larger than the  $20 \text{ cm}^2$   
 282  $\text{s}^{-2}$  average value in the region downstream where eddy activity was weak (between 35°E  
 283 to 40°E and 52.5°S to 54°S; Figure 2a). Vigorous currents dominated the first part of  
 284 the deployment in the high-EKE region near the standing meander (yeardays 120-155),  
 285 which presented challenges for keeping the autonomous platforms together (Figure 2c).  
 286 In the low-EKE region downstream, during the latter portion of the deployment (year-  
 287 days 170-206), the gliders sampled across at least one coherent eddy and the gliders and  
 288 float remained in close proximity (Figure 2c). Throughout the sampling period, the air-  
 289 sea heat flux was characterized by net surface cooling that led to a slow thickening of  
 290 the mixed layer; details of the surface forcing are provided in Figure 3.

291 Mean hydrographic properties computed from Argo float observations (Roemmich  
 292 & Gilson, 2009) and measurements from the I06S repeat transect at 30°E show the dom-  
 293 inance of the PF in setting large-scale tracer distributions in this region (Figure 4). Lo-  
 294 cated at approximately 51°S, the PF is associated with a region of outcropping density  
 295 surfaces. In the upper 400 m of the water column, the PF acts as a barrier to mixing  
 296 between warmer waters to the north and cooler waters to the south that have a tem-  
 297 perature minimum at a depth of 150-200 m (Figure 4a). The PF also separates southern,  
 298 salinity-stratified waters from temperature-stratified waters to the north (Stewart & Haine,  
 299 2016). The salinity distribution shows evidence of subduction of fresher waters along den-  
 300 sity surfaces at the core of the PF, illustrating that on large scales, this region is asso-  
 301 ciated with ventilation of intermediate waters (Figure 4b). Patterns in backscatter mir-  
 302 ror the temperature distribution, with colder waters to the south showing a local min-  
 303 imum in backscatter near 150 m depth and the PF marking the southern boundary of  
 304 high surface backscatter values to the north (Figure 4d).

305 The core of the PF is associated with a local weakening of the stratification at the  
 306 base of the mixed layer, which likely enables subduction in this region (Figure 4c). Near  
 307 the PF, stratification at the base of the mixed layer is strongest and the MLD itself shal-  
 308 lowest at the end of the austral summer (March), as a result of the stratifying effects of  
 309 sea ice melt and increased solar radiation (Giddy et al., 2021). During austral fall and  
 310 early winter (April-July), stratification at the base of the mixed layer decreases, corre-  
 311 sponding to a reduction in the maximum vertical stratification (Dong et al., 2008). The  
 312 autonomous platforms sampled during this weakening of the stratification in austral fall,  
 313 which is also consistent with the surface forcing over the deployment period (Figure 3).

### 314      3.2 High-resolution physical and biogeochemical observations

315      Despite their relative proximity, the distributions of temperature-salinity ( $\theta - S$ )  
 316      values measured by the float and by the gliders differ significantly. Throughout the de-  
 317      ployment, the float sampled a relatively tight  $\theta - S$  relationship, reflecting properties  
 318      of the PF core waters (temperatures between 2°C and 2.5°C; Figure 5a). This suggests  
 319      the float's trajectory was Lagrangian to good approximation, despite profiling vertically.  
 320      While the gliders spent a large portion of time sampling within the PF core waters as  
 321      well, they also observed water masses sourced from north of the PF (with higher SSH  
 322      and temperatures warmer than 2.5°C) and from south of the PF (with lower SSH and  
 323      temperatures colder than 2°C). The gliders sampled a larger range of water mass prop-  
 324      erties during the first part of the deployment, corresponding to the high-EKE region (Fig-  
 325      ure 5b). Despite our best efforts to keep the gliders close to the float during the deploy-  
 326      ment, the platforms did not sample identical water masses over the duration of the mis-  
 327      sion. In some places this reflects the strong frontal currents and associated abrupt changes  
 328      in water properties, although the platforms were geographically distant at certain times  
 329      as well (Figure 2c). In fact, the gliders at times sampled “southern-sourced” waters based  
 330      on hydrographic properties despite being physically well north of the float (Figure 2b,  
 331      e.g. yeardays 130-150) – a signature of lateral stirring across the PF.

332      Gaps in  $\theta - S$  space found in the distribution of hydrographic properties are in-  
 333      dicative of multiple small-scale fronts (Naveira Garabato et al., 2011). This frontal struc-  
 334      ture is also supported by consideration of the local SSH field along the path of the glid-  
 335      ers. Multiple minima in the frequency distribution of SSH are indicative of the gliders  
 336      sampling across more than one frontal jet (Sokolov & Rintoul, 2009; Thompson & Sallée,  
 337      2012). In the high-EKE region early in the study period, the gliders sampled across sev-  
 338      eral water masses separated by multiple fronts (Figure 5b,c). This frontal structure is  
 339      highlighted further in Figure 8a, which shows that  $\theta - S$  properties are correlated with  
 340      SSH in the high-EKE region. In the standing meander region, mesoscale eddies may form  
 341      and enclose water properties from either side of the front (Thompson & Sallée, 2012; Roach  
 342      et al., 2016). This makes it difficult to distinguish jets from eddies in the glider data, al-  
 343      though the correlation between SSH and  $\theta - S$  will primarily reveal mesoscale structure  
 344      due to the resolution of the altimetry data. In contrast, in the low-EKE portion of the  
 345      deployment, distinct water masses were only sampled when crossing eddies shed from  
 346      the PF (Figure 5d). During this latter period, the low range of SSH values sampled, to-  
 347      gether with the quasi-Lagrangian nature of the float, suggest that the gliders and float  
 348      both stay primarily within the PF core waters. Over the full deployment, the PF core  
 349      waters were observed most frequently (Figure 5e).

350      The similarities and differences in tracer variability between the high-EKE and low-  
 351      EKE regions is further illustrated by the representative depth-time series plots of phys-  
 352      ical and biogeochemical properties from one of the gliders (SG660) shown in Figures 6  
 353      and 7. Periods dominated by mesoscale variability are characterized by homogeneous prop-  
 354      erties in the upper 500 m of the water column as well as curvature in the isopycnals that  
 355      is anti-correlated with SSH, for example during yeardays 140-145 (Figures 6a, 7a,b). Cor-  
 356      related variations between the vertical displacement of isopycnals and SSH are not ob-  
 357      served to the same extent in the low-EKE regime, although the signature of a mesoscale  
 358      eddy is present in the tracer observations collected between days 187-194 (Figure 6e-h).  
 359      Higher frequency and finer scale variability also occurs at the typical glider sampling scale,  
 360       $O(<1 \text{ day}, <10 \text{ km})$ , throughout the time series. This submesoscale variability is enhanced  
 361      along the periphery of the mesoscale structures, consistent with increased strain in these  
 362      regions (Brannigan, 2016; Siegelman, 2020). These features are particularly noticeable  
 363      in temperature (Figure 6a,e), which acts as a passive tracer below the mixed layer, as  
 364      well as in oxygen and optical backscatter (Figure 6c,g and d,h). Outside of the coher-  
 365      ent mesoscale features, in what is sometimes referred to as the “submesoscale soup” (McWilliams,  
 366      2016), fine-scale tracer variability appears as horizontal layers, primarily in the high-EKE

region (Figure 6a,c,e,g). Notably, the MLD is more variable in the high-EKE region, shoaling particularly at the edges of mesoscale eddies, and then stays relatively constant in the low-EKE region (black line in Figure 6a,b).

The optical backscatter distribution is closely correlated with temperature, with warmer temperatures associated with higher backscatter values (Figure 6d,h, 470 nm wavelength; sections of the 700 nm backscatter are similar but not shown). The temperature-backscatter relationship is consistent with the large-scale distribution observed during the I06S cruise (Figure 4d), suggesting that in both of these properties, stirring cascades variance to smaller scales. An compelling feature of both the temperature and backscatter data is the non-monotonic vertical distribution, with the presence of prominent low anomalies located just below the mixed layer in the high-EKE region, sandwiched between higher values above and below (yeardays 127-132 and yeardays 145-150, between 150 m to 250 m). The temperature minima could be explained as a remnant of cold Winter Water that is capped in the summer by a warmer surface layer. In contrast, the backscatter mimima must arise from lateral or along-isopycnal advection. For instance, this feature could arise from the subduction of cold surface waters with low backscatter sourced from south of the PF. Notably, the backscatter minima at the base of the mixed layer (at approximately 150 m) only occurs in the high-EKE region, even though in the downstream region backscatter has a similar correlation with temperature at mesoscales (see mesoscale features over yeardays 132-135 and 187-195).

There is generally strong stratification at the base of the mixed layer throughout the deployment, which may limit exchange between the surface boundary layer and the ocean interior (Figure 7c,g). However, in the high-EKE region, the glider encountered intermittent periods of weakened upper ocean stratification collocated with the edge of strong mesoscale features. Although there is little evidence for coherent boluses of weakly stratified, low PV waters in the interior, high PV waters with strong stratification are observed to intrude into the mixed layer in the high-EKE region (e.g., yeardays 125, 132, and 136; Figure 7d,h). The advection of high PV waters towards the surface is reminiscent of the tracer distributions associated with upwelling induced by anticyclonic eddies in the model-based study of Brannigan (2016) (their Figure 2).

The complicated three-dimensional circulation that the gliders sampled along their trajectories motivates a consideration of biogeochemical distributions in temperature-salinity space as well as geographic space. Optical backscatter distributions, despite the intricate variations along the gliders' trajectories (Figure 6d,h), are largely shaped by the frontal structure in this region, with elevated backscatter values found north of and in the core of the PF and considerably lower backscatter values to the south (Figure 8c). Regions with high surface backscatter values do not all have the same vertical distributions; backscatter values are elevated to much greater depths and density classes for those waters associated with the core of the PF (Figure 8c,d). This suggests that subduction of water with high backscatter values (and potentially high POC) is linked to specific water masses and water mass formation processes.

The distribution of AOU also shows distinct behaviors between the different frontal regions. South of the PF core waters, contours of AOU (in temperature-salinity space) are predominantly aligned with contours of spice (Figure 8b). The resulting gradient of AOU on density surfaces may arise from lateral advection as cold anomalies are correlated with low AOU/high dissolved oxygen anomalies. This suggests that these waters have recently been subducted to the south of the study region, since these density classes do not access the mixed layer in the float/glider observations. North of and within the PF core waters, contours of AOU are largely aligned with density contours, such that AOU increases with depth and density. Those density surfaces with low AOU anomalies south of the PF have higher AOU values north of the PF, suggesting that recently ventilated waters are localized to the PF.

419            **3.3 Submesoscale structures**

420            Submesoscale motions are typically enhanced in the ocean surface boundary layer  
 421 due to reduced stratification and the potential for frontogenesis (Thomas et al., 2008;  
 422 McWilliams, 2016). Characterization of mixed-layer frontal structure has been a com-  
 423 mon method for assessing the potential for submesoscale motions and instabilities (Thompson  
 424 et al., 2016), with previous studies showing that the statistical properties of the mixed  
 425 layer can change over relatively short spatial scales (Viglione et al., 2018). In the SO-  
 426 GOS glider data, strong lateral buoyancy gradients in the along-track direction form in  
 427 the mixed layer in the high-EKE region, as disparate water masses are stirred together  
 428 (Figure 9). Both temperature and salinity anomalies in the surface layer work in con-  
 429 cert to enhance the buoyancy anomalies. The compounding contributions from temper-  
 430 ature and salinity intensify lateral buoyancy gradients when these water masses are stirred  
 431 by mesoscale eddies (for example, on yeardays 124, 139, 146, and 149; Figure 9b). Lat-  
 432 eral buoyancy gradients have peak magnitudes and are most variable during the initial  
 433 month of the deployment (Figure 9d). Strong surface buoyancy gradients are collocated  
 434 with the edge of coherent mesoscale eddies or small-scale fronts, which are commonly  
 435 associated with an intermittent shoaling of the mixed layer on the time scale of 1-2 glider  
 436 dives ( $\approx$ 3-10 hours). The magnitude of the mixed-layer lateral buoyancy gradient weak-  
 437 ens over the duration of the deployment (Figure 9d). This weakening could be caused  
 438 by seasonal-scale changes in surface forcing (Figure 3a); however, the fact that the MLD  
 439 remains relatively uniform (Figure 9c) suggests that it is more likely related to the re-  
 440 duction in vigorous stirring by mesoscale motions later in the deployment.

441            The prevailing paradigm for ventilation of the surface mixed layer by submesoscale  
 442 motions has been along-isopycnal subduction at fronts, moving water masses across the  
 443 base of the mixed layer (Ruiz et al., 2009; Omard et al., 2015; Freilich & Mahadevan,  
 444 2019). This view has been supported by consideration of tracer distributions in density  
 445 space, in which tracer anomalies tend to be aligned along isopycnals, even if they have  
 446 a significant vertical structure (see Fig. 3 in Lévy et al. (2018), for instance). In the glider  
 447 observations, there are significant variations in spice and AOU along density surfaces,  
 448 and anomalies are also often coherent across a broad range of densities, particularly be-  
 449 low the mixed layer (Figure 10). The lack of obvious, coherent along-isopycnal subduc-  
 450 tion events indicates that other processes are active or that the subduction features oc-  
 451 cur at small scales so that gliders only observe them intermittently. Consistent with Fig-  
 452 ure 8b, AOU and spice anomalies are tightly correlated in regions associated with cold,  
 453 southern-sourced waters. Anomalies in both spice and AOU echo the signatures of mesoscale  
 454 features seen in Figures 6 and 7. At eddy peripheries or between eddies, most notice-  
 455 able where there is a strong tilting of density surfaces (e.g. day 124 or 140), there are  
 456 enhanced submesoscale variations (Siegelman, 2020). In these regions, both spice and  
 457 AOU anomalies are coherent across a broad range of densities, even well below the base  
 458 of the mixed layer, which suggests that stirring by (largely barotropic) eddies is likely  
 459 the primary mechanism for generating this structure. Smaller-scale variations on den-  
 460 sity surfaces exist primarily in the high-EKE region, suggesting that in this region, deep  
 461 density classes are accessed by filamentary structures that transport tracers vertically.

462            Although tracer anomalies are not predominantly aligned with density surfaces, the  
 463 signature of surface mixed layer-interior exchange is apparent nonetheless. In several lo-  
 464 cations throughout the deployment, low AOU (recently ventilated) waters intrude well  
 465 below the MLD (Figure 10). Most notably, between yeardays 148-152, recently venti-  
 466 lated waters reach density surfaces typically associated with Upper Circumpolar Deep  
 467 Water ( $> 27.6 \text{ kg/m}^3$ ). In addition to the observations of low spice, low AOU waters ex-  
 468 tends to denser isopycnals, there is also evidence of deep, oxygen-depleted (high AOU)  
 469 waters reaching across the base of the mixed layer (yearday 140), consistent with high-  
 470 stratification waters intruding into the mixed layer at eddy peripheries in Figure 7c.

### 471      3.4 Biological signatures

472      While we have thus far focused on physical processes that generate the variability  
 473      observed in both physical and biogeochemical tracer distributions, biological variability  
 474      was also apparent in the glider and float data. Spikes in backscatter can be signatures  
 475      of aggregated particulates (Briggs et al., 2011, 2020). Typically the export of ag-  
 476      gregates is dominated by gravitational sinking, rather than by active advective processes  
 477      that contribute to the export of smaller particles (Boyd et al., 2019). The number of ag-  
 478      gregated particles, counted by large spikes in the  $b_{bp}$ , is variable across the deployment  
 479      but is often correlated with the concentration of backscatter in the mixed layer, consis-  
 480      tent with the export process for large particulate aggregates being primarily one-dimensional  
 481      (Figure 11a,b). The regions of highest backscatter at the surface are correlated with warmer  
 482      waters sourced north of the PF (*e.g.* yeardays 120-122 and 130-140). While large aggre-  
 483      gates may sink out of the water column, smaller non-aggregated particulate matter may  
 484      be transported along isopycnals to intermediate depths (Dever et al., 2021), a process  
 485      that highlights the impact of three-dimensional transport on tracer distributions.

486      The float backscatter data, which were collected to greater depth than that col-  
 487      lected by the gliders, reveal that enhanced backscatter can exist at depths down to 600 m  
 488      in the high-EKE region (not shown). Although the platforms did not follow identical path-  
 489      ways and backscatter processing between the platforms differ, the distribution of spikes  
 490      in 700 nm backscatter from float WMO 5906030 is qualitatively similar to that deter-  
 491      mined from the gliders (Figure 11a). However, due to the 5-day sampling period of the  
 492      float, the small-scale structure within the patterns in the glider backscatter spike data  
 493      is absent in the float backscatter data, which can have a significant impact on longer-  
 494      term mean values. Observing platforms that rely on sampling on the order of many days  
 495      will miss this high-frequency variability, which provides information on particulate ex-  
 496      port from the surface ocean, especially due to submesoscale dynamics.

497      Backscatter spectral slope ( $\gamma_{b_{bp}}$ ), which was calculated using two wavelengths of de-  
 498      spiked backscatter from  $b_{bp}(\lambda) = b_{bp}(\lambda_0) \frac{\lambda}{\lambda_0}^{-\gamma_{b_{bp}}}$ , has been shown to reflect the size dis-  
 499      tribution of suspended particles (Kostadinov et al., 2009; Dever et al., 2021). Qualita-  
 500      tively, the spectrum of backscatter will flatten as the percentage of larger particles in-  
 501      creases; a transition from large to small  $\gamma_{b_{bp}}$  may thus indicate a transition into a more  
 502      productive region with larger phytoplankton. Estimates from satellite observations of  
 503       $\gamma_{b_{bp}}$  in the surface ocean of the Southern Ocean suggest values of 0.5-1.5 (Loisel et al.,  
 504      2006), consistent with our glider estimates.

505      Ranging from 0 to 4,  $\gamma_{b_{bp}}$  is generally low in the surface mixed layer (Figure 11c),  
 506      suggesting a greater proportion of large-sized particles that are potentially diatoms, the  
 507      dominant marine primary producers in the Southern Ocean (de Baar et al., 1999; Rousseaux  
 508      & Gregg, 2014). Below the mixed layer,  $\gamma_{b_{bp}}$  increases, particularly in regions where backscat-  
 509      ter concentrations are low (*e.g.* yeardays 146-147, 178-196); here a larger proportion of  
 510      small-sized particles are likely dominating the backscatter measurements. In general, the  
 511      high-EKE region has a weaker vertical gradient in  $\gamma_{b_{bp}}$  across the base of the mixed layer,  
 512      suggestive of enhanced surface-interior exchange.

513      The particle composition distribution suggests plankton communities with differ-  
 514      ing compositions are intricately mixed in this localized region of high EKE in the South-  
 515      ern Ocean. The PF typically acts as a barrier to mixing of biological communities and  
 516      is a known front in silicate, which has implications for the growth of diatoms (Freeman  
 517      et al., 2018). However, the high EKE at standing meanders may allow plankton com-  
 518      munities to be stirred into proximity and ultimately to mix. While these communities  
 519      remain intact when transported within coherent mesoscale features (*e.g.* days 178-196  
 520      in Figure 11c), mixing of these communities occurs in filaments at the edges of eddies.  
 521      Such mixing is especially prevalent in the high-EKE region, implying a regional hotspot  
 522      for community mixing both in the surface ocean and at depth (Figure 11c).

523 **4 Discussion**

524 **4.1 Cross-scale contributions to variability**

525 Our understanding of the role of mesoscale and submesoscale processes in setting  
 526 the distribution of biogeochemical tracers has been shaped by observations of organic  
 527 matter subduction (Mahadevan, 2016; Stukel & Ducklow, 2017), as well as heavily-instrumented  
 528 studies that tracked the transport of tracer anomalies between the surface ocean and the  
 529 interior (Omand et al., 2015; Stukel et al., 2017). However, open questions remain about  
 530 the relative contributions that processes at different scales make to setting these patterns.  
 531 This is particularly true in the Southern Ocean where observational surveys that resolve  
 532 submesoscale features have been rare (Adams et al., 2017), and geographic regions or  
 533 features that enhance export via small-scale subduction remain relatively unexplored.

534 Stirring by mesoscale eddies is known to produce filaments and anomalies of spice,  
 535 AOU, and biogeochemical tracers at smaller submesoscales, particularly in regions where  
 536 water masses with differing formation processes and community compositions are adja-  
 537 cent (Smith & Ferrari, 2009; Balwada et al., 2018, 2020). In the Southern Ocean, the  
 538 PF supports large gradients in temperature and salinity that, via stirring by geostrophic  
 539 turbulence, can produce a direct cascade of tracer variance to small scales, especially be-  
 540 low the mixed layer. Indeed, the largest variance of tracers occurs on density surfaces  
 541 below the mixed layer and can be explained primarily by stirring of large-scale gradi-  
 542 ents at the mesoscale, particularly within the high-EKE standing meander region (Fig-  
 543 ures 8 and 12). Furthermore, the majority of the observed tracer features at the subme-  
 544 sesoscale are not aligned along density surfaces. Thus, vigorous stirring along tilted den-  
 545 sity surfaces, ubiquitous in the Southern Ocean and particularly at the PF, must be crit-  
 546 ical in assisting with the export of biologically-relevant tracers from the surface layer to  
 547 the interior. To this end, parameterizations that assume purely vertical sinking for par-  
 548 ticular matter may misrepresent the subduction of organic matter in the Southern Ocean,  
 549 particularly due to the three-dimensional structure of high EKE and enhanced stirring.

550 Yet, these observations also provide evidence that submesoscale motions are likely  
 551 impacting surface boundary layer-interior exchange. This is particularly true for waters  
 552 sourced from north of the PF, for which tracers such as AOU are more aligned with den-  
 553 sity surfaces (Figure 8b). Furthermore, high AOU and spice anomalies that reach across  
 554 the base of the mixed layer occur almost exclusively along the periphery of coherent mesoscale  
 555 features, as distinguished by co-variations in SSH and density surfaces. More broadly,  
 556 stirring along density surfaces may also generate strong vertical gradients across the base  
 557 of the mixed layer that then increase tracer fluxes due to turbulent vertical mixing at  
 558 the submesoscale. Observations with high spatial and temporal resolution, sampled in  
 559 a way that crosses submesoscale fronts at a near-perpendicular angle, are necessary for  
 560 inferring ageostrophic vertical velocity  $w$  from existing parameterizations. While we were  
 561 not able to provide a direct estimate of  $w$  with this dataset, there is strong evidence that  
 562 upper-ocean submesoscale motions are playing a role in the subduction of surface wa-  
 563 ters, in a compact region in the lee of topography. Our observations thus allow for the  
 564 validation of models that predict enhanced vertical tracer exchange where submesoscale  
 565 dynamics are active. Ultimately, because features at the submesoscale are shaped by the  
 566 mesoscale, the coupling of these scales plays an important role in shaping the tracer gra-  
 567 dient, with submesoscales having a more prominent role in enabling exchange across the  
 568 base of the mixed layer and mesoscales shaping tracer distributions at depth.

569 Isolating physical mechanisms responsible for tracer distributions becomes chal-  
 570 lenging when constrained solely by vertical profiles from floats that sample every  $O(10$   
 571 days). Higher-resolution glider measurements, which sample scales of  $O(\text{hours}, 1 \text{ km})$ ,  
 572 provide greater insight into anomalies resulting from mesoscale stirring and active sub-  
 573 mesoscale processes, which may be either misclassified or entirely absent in typical float  
 574 profiles. Figure 13 shows how the BGC-Argo float and the gliders sampled around the

edge of a mesoscale eddy in the low-EKE region of the deployment. The quasi-Lagrangian float was advected cyclonically around the edge of the eddy, performing three purely vertical profiles. In contrast, the glider sampled across the edge of the eddy and crossed through a coherent, low-AOU anomaly that extended below the mixed layer to a depth of 400 m, likely indicative of waters recently subducted from the surface layer (Figure 13a). The feature was not clearly observed by the float although the instruments were all within 20 km of each other (Figures 2c, 13b). In fact, both gliders crossed the mesoscale eddy edge, but only one observed the submesoscale subduction feature, highlighting the azimuthal variability around a given eddy. Llort et al. (2018) showed that, in high-EKE regions of the Southern Ocean, anomalies of spice and AOU at depth are regularly present in BGC-Argo float profiles and described a method to attribute such anomalies to submesoscale dynamics. Our data illustrate that an accurate interpretation of profiling float observations must account for the fact that small numbers of floats will not capture the full signature of the submesoscale, particularly because these instruments do not often cross eddy edges. To this end, parameterizations that assume purely vertical sinking for particulate matter may misrepresent the subduction of organic matter in the Southern Ocean, particularly due to the three-dimensional structure of of high EKE and enhanced stirring.

#### 4.2 The case for Southern Ocean ventilation hotspots

Standing meanders of the Southern Ocean, characterized by high EKE and rates of strain, may play an outsized role in the export of organic matter due to their ability to sustain a persistent and vigorous mesoscale eddy field that provides a source of frontogenesis and catalyzes strong submesoscale motions that enhance vertical velocities and fluxes (Siegelman, 2020). Our data set is unique in that the gliders and float sampled regions of both strong and weak mesoscale strain, corresponding roughly to the first and second halves of the deployment, respectively (Figure 2a). Evidence for subduction at the submesoscale is greater in the high-EKE portion of our study region, where larger lateral buoyancy gradients, stronger tracer variability, and high oxygen values penetrating deeper into the water column are all diagnostics consistent with enhanced submesoscale activity (Figures 9 and 10). The MLD is both shallower on average and more variable in the high-EKE region (Figure 9), potentially demonstrative of shoaling as a result of mixed layer instability (Thompson et al., 2016; du Plessis et al., 2017; Viglione et al., 2018). This observation is also consistent with numerical models, such as Balwada et al. (2018), that find that mixed layers are shallower downstream of a topographic feature where an active submesoscale field is present. Finally, the deepest penetration of the backscatter data away from the surface is found within the core of the PF, associated with the strongest frontal structure (Figure 8c).

Further evidence for localized ventilation in the standing meander is the stronger along-isopycnal tracer variance in the high-EKE region directly in the lee of topography than in the low-EKE region downstream (Figure 12). The difference in tracer variance between the high- and low-EKE regions is particularly apparent on isopycnals with average depths of 250-500 m. At times these isopycnals reach close to the base of the mixed layer, and thus this variance can influence the exchange of tracers between the interior ocean and the surface layer. The peak in variance is deeper in the high-EKE region (350 m) compared to the low-EKE region (250 m). In contrast to these mid-depth isopycnals, anomalies are low on isopycnals found in the surface ocean because of the homogenizing nature of the mixed layer (the average MLD is 140 m). These tracer variance characteristics suggest that vigorous stirring by coherent eddies within the standing meander plays a dominant role in setting tracer distributions and gradients in the interior ocean. Furthermore, the peak in tracer variance occurs at greater depths in the high-EKE region as compared to downstream, despite deeper mixed layers in the latter (Figure 12). While much of the tracer variance generation likely occurs through mesoscale stirring,

627 injection of anomalously low AOU, low spice waters from the surface is required to main-  
 628 tain the range of observed tracers.

629 While small-scale fluctuations in the stratification at the base of the mixed layer  
 630 are observed by the glider (Figure 7c,g), overall there is only a slight difference in the  
 631 maximum value of stratification ( $N_{max}^2$ ) between the high-EKE standing meander and  
 632 the low-EKE downstream region. In the high-EKE region, both  $N_{max}^2$  (Figure 14a) and  
 633 lateral buoyancy gradients in the mixed layer (Figure 14b) are slightly stronger, but by  
 634 less than a factor of 2. In contrast, substantial changes are found in the vertical tracer  
 635 gradient across the base of the mixed layer (shown as a change in spice in the 10 m above  
 636 and below the depth of  $N_{max}^2$  in Figure 14), with gradients within the high-EKE region  
 637 reduced by almost an order of magnitude as compared to those in the low-EKE region.  
 638 Weaker vertical gradients in tracers suggest that those waters were recently subducted  
 639 below the mixed layer. While gradients of spice can possibly be impacted by seasonal  
 640 or meridional changes, the signal of reduced vertical tracer gradients is also robust in AOU,  
 641 which has a relatively constant value near the surface. Waters between the depth of  $N_{max}^2$   
 642 and the depth of  $N_{max}^2 + 200$  m in the high-EKE region are substantially more likely to  
 643 have lower values of AOU than those in the low-EKE region, suggesting these waters have  
 644 been more recently ventilated and subducted below the depth of high stratification, po-  
 645 tentially via active submesoscale processes (Figure 15). Whether this alignment of in-  
 646 creased ventilation with higher EKE is a pattern that holds across the Southern Ocean  
 647 remains an interesting open question.

648 In this data set, there is only weak evidence for the subduction of low PV (weak  
 649 stratification) anomalies into the interior. This can be contrasted with the intense sur-  
 650 face boundary layer-interior exchange that has been observed in the wintertime North  
 651 Atlantic (Thompson et al., 2016). This characteristic of the SOGOS data differs from  
 652 a recent study by Bachman and Klocker (2020), in which an extremely high-resolution  
 653 simulation (1/120°) was employed to argue that topographically-steered jets produce lo-  
 654 calized regions of enhanced ventilation. These simulations, focused on the region around  
 655 the Kerguelen Plateau, produced a strong stationary jet north of the plateau, with sur-  
 656 face velocities and EKE variations similar to our study region. Focusing on the topographically-  
 657 steered jet, Bachman and Klocker (2020) suggested that a westerly wind stress can pro-  
 658 duce a destabilizing Ekman buoyancy flux that generates convective mixing and intense  
 659 exchange with the interior (Thomas & Lee, 2005). Most diagnostics in this study do not  
 660 extend into the standing meander region just downstream of the plateau. While we can  
 661 not rule out the possibility that a similar mechanism occurs as the PF passes directly  
 662 over the SWIR, the float and the gliders all measure stratification levels at the base of  
 663 the mixed layer that are much greater than one would expect if convective mixing was  
 664 active. Our observations suggest instead that ventilation peaks as the jet becomes more  
 665 variable and filamented in the lee of topography and mesoscale stirring intensifies.

666 Considering the SOGOS observations in the context of our current understanding  
 667 of the Southern Ocean, a picture emerges where instabilities associated with topographically-  
 668 steered jets give rise to an energetic field of mesoscale eddies. The jet itself has enhanced  
 669 gradients in tracer properties that are then effectively stirred in the standing meander.  
 670 This stirring strengthens horizontal surface buoyancy gradients, leading to an active sub-  
 671 mesoscale velocity field. The depth to which these submesoscale motions penetrate is  
 672 difficult to determine from our observations but likely depends strongly on the strati-  
 673 fication at the base of the mixed layer. During our study period, this stratification ap-  
 674 pears to be relatively strong due to the influx of freshwater and low mean wind stress.  
 675 Intermittent, strong wind events ( $> 0.5 \text{ N m}^{-2}$ ) did occur several times over the glider  
 676 deployment (Figure 3c), which may have acted to destabilize the mixed layer, similar to  
 677 the results of Bachman and Klocker (2020) or Giddy et al. (2021). However, even if the  
 678 submesoscale tracer fluxes are localized to the surface ocean, they still provide a con-  
 679 tinuous source of recently ventilated surface waters that are effectively stirred by the mesoscale,

generating fine-scale gradients along density surfaces. Thus, through a combination of mesoscale stirring and submesoscale fluxes in the surface boundary layer, exchange between the surface ocean and the interior may be enhanced.

Observations such as those described here, together with model simulations, have suggested that standing meanders in the ACC may play an outsized role in air-sea exchange as well as tracer exchange between the surface and interior ocean. Process studies have demonstrated that this exchange is dependent on dynamics at the mesoscale and submesoscale and that along-stream variability created by standing meanders can result in vital regions of subduction and ventilation. Enhanced vertical velocities and vigorous stirring result in increased tracer variability that can lead to highly localized ventilation of old waters; in turn, localized ventilation impacts air-sea fluxes due to a disequilibrium between the atmosphere and surface ocean carbon dioxide ( $\text{pCO}_2$ ) concentrations. Year-round data from BGC-Argo floats have allowed for further investigation into the locations of carbon uptake and outgassing in the ACC. These float-based estimates show that the regions around the Polar Front exhibit significant outgassing during autumn and winter, likely associated with the large-scale upwelling of old, carbon-rich waters (Gray et al., 2018). The development and deployment of unmanned surface vehicles has further expanded the collection of  $\Delta\text{pCO}_2$  concentrations across the atmosphere and surface ocean (Sutton et al., 2021). However, the role of localized regions of enhanced EKE has not yet been diagnosed using such methods, in terms of the effects on air-sea exchange of  $\text{CO}_2$ . Previous model-based work that considered the distribution and number of platforms needed to constrain air-sea fluxes in the Southern Ocean found that high-frequency variance dominated in topographically complex locations (Mazloff et al., 2018; Wei et al., 2020), suggesting that increased sampling rates in those regions would be a valuable tool for constraining Southern Ocean tracer budgets. Due to the potential importance of these regions in impacting air-sea fluxes, observing systems in the Southern Ocean should consider using an adaptive sampling strategy for these regions, increasing sampling rates when platforms enter these standing meanders. Higher rates of sampling in standing meanders of the ACC may lead to a more complete understanding of their role in the carbon cycle and also provide year-round data regarding strength of subduction and ventilation at the mesoscale and submesoscale.

## 5 Conclusions

Data from a pair of ocean gliders, deployed alongside a SOCCOM BGC-Argo float, are used to assess the scales of variability in physical and biogeochemical tracers both within and downstream of a major standing meander of the ACC's Polar Front. In both regions, variability in passive tracers is largest along the edge of coherent mesoscale eddies. However, the standing meander, marked by enhanced EKE and strain, exhibits enhanced lateral buoyancy gradients in the mixed layer, a more variable MLD, and evidence of stronger interior mesoscale stirring, as compared to the more quiescent downstream region. Despite similar mean vertical stratification in both parts of the deployment, vertical tracer gradients are nearly an order of magnitude weaker in the standing meander region, suggesting more efficient subduction of surface waters into the interior. While submesoscale motions are likely critical for carrying tracer anomalies across the base of the mixed layer, interior stirring effectively advects these tracers to depth in the standing meander.

The observations presented here confirm a series of recent high-resolution modeling studies (Rosso et al., 2015; Balwada et al., 2018; Bachman & Klocker, 2020) that highlighted the key role that the complex three-dimensional stirring occurs downstream of the interaction of the PF with topography has on vertical exchange between the surface ocean and interior. These regions are characterized as having an active submesoscale flow field with vigorous restratification processes occurring in a region of high EKE. Filamentary structures that allow for the vertical movement of tracers impact the transport of

732 organic matter into the interior ocean, as well as the ventilation of older waters found  
 733 at depth in the Southern Ocean. There are a discrete number of standing meanders as-  
 734 sociated with high EKE along the path of the ACC, each of which is likely to be a key  
 735 region of surface-interior exchange that impacts air-sea exchange and biogeochemical cy-  
 736 cling. Our results highlight the need for improved focus on parameterizing flow-topography  
 737 interactions in models with coarse resolution. Ventilation in the ACC's standing mean-  
 738 ders is highly localized, typically spanning a region of only a few hundred kilometers, in  
 739 which Lagrangian floats experience a short residence time, even with a 1000-m parking  
 740 depth. To address the impact of standing meanders on large-scale air-sea carbon fluxes  
 741 in the Southern Ocean, current and future observational systems should consider em-  
 742 ploying adaptive sampling in these regions.

### 743 Acknowledgments

744 We are grateful to the captain and crew of the R/V Thomas G. Thompson as well as  
 745 A. Orsi, L. Talley, I. Rosso, G. Viglione, and M. Kotz for their assistance in deploying  
 746 the gliders during the 2019 I06S GO-SHIP cruise. We thank D. Swift, S. Riser, and the  
 747 SOCCOM executive team for increasing sampling frequency of the BCG-Argo float dur-  
 748 ing the SOGOS mission. LAD and AFT were supported by NSF award OCE-1756956  
 749 and the David and Lucille Packard Foundation. LAD was additionally supported by an  
 750 NSF Graduate Research Fellowship. DB and ARG were supported by NSF award OCE-  
 751 1756882; ARG received additional support from NASA through award NNX80NSSC19K1252  
 752 and from the U.S. Argo Program through NOAA grant NA15OAR4320063.

753 The glider data are archived at NOAA's National Centers for Environmental in-  
 754 formation and can be accessed at <https://www.ncei.noaa.gov/archive/acquisition/0228185> and <https://www.ncei.noaa.gov/archive/acquisition/0228187>. Data from  
 755 the BGC-Argo float were collected and made freely available by the Southern Ocean Car-  
 756 bon and Climate Observations and Modeling (SOCCOM) Project funded by the National  
 757 Science Foundation, Division of Polar Programs (NSF PLR-1425989 and OPP-1936222),  
 758 supplemented by NASA, and by the International Argo Program and the NOAA pro-  
 759 grams that contribute to it. (<http://www.argo.ucsd.edu>, <http://argo.jcommops.org>).  
 760 The Argo Program is part of the Global Ocean Observing System.  
 761

### 762 References

- 763 Adams, K. A., Hosegood, P., Taylor, J. R., Sallée, J.-B., Bachman, S., Torres, R., &  
 764 Stamper, M. (2017). Frontal Circulation and Submesoscale Variability dur-  
 765 ing the Formation of a Southern Ocean Mesoscale Eddy. *Journal of Physical  
 766 Oceanography*, 47(7), 1737–1753. doi: 10.1175/JPO-D-16-0266.1
- 767 Bachman, S. D., & Klocker, A. (2020). Interaction of Jets and Submesoscale Dy-  
 768 namics Leads to Rapid Ocean Ventilation. *Journal of Physical Oceanography*,  
 769 50(10), 2873–2883. doi: 10.1175/JPO-D-20-0117.1
- 770 Bachman, S. D., Taylor, J. R., Adams, K. A., & Hosegood, P. J. (2017). Mesoscale  
 771 and Submesoscale Effects on Mixed Layer Depth in the Southern Ocean. *Jour-  
 772 nal of Physical Oceanography*, 47(9), 2173–2188. doi: 10.1175/JPO-D-17-0034  
 773 .1
- 774 Balwada, D., LaCasce, J. H., Speer, K. G., & Ferrari, R. (2020). Relative Disper-  
 775 sion in the Antarctic Circumpolar Current. *Journal of Physical Oceanography*,  
 776 -1 (aop). doi: 10.1175/JPO-D-19-0243.1
- 777 Balwada, D., Smith, K. S., & Abernathey, R. (2018). Submesoscale Vertical  
 778 Velocities Enhance Tracer Subduction in an Idealized Antarctic Circum-  
 779 polar Current. *Geophysical Research Letters*, 45(18), 9790–9802. doi:  
 780 10.1029/2018GL079244
- 781 Balwada, D., Speer, K. G., LaCasce, J. H., Owens, W. B., Marshall, J., & Ferrari,  
 782 R. (2016). Circulation and Stirring in the Southeast Pacific Ocean and the

- 783       Scotia Sea Sectors of the Antarctic Circumpolar Current. *Journal of Physical*  
 784       *Oceanography*, 46(7), 2005–2027. doi: 10.1175/JPO-D-15-0207.1
- 785       Boccaletti, G., Ferrari, R., & Fox-Kemper, B. (2007). Mixed Layer Instabilities and  
 786       Restratification. *Journal of Physical Oceanography*, 37(9), 2228–2250. doi: 10  
 787       .1175/JPO3101.1
- 788       Bol, R., Henson, S. A., Rumyantseva, A., & Briggs, N. (2018). High-Frequency Vari-  
 789       ability of Small-Particle Carbon Export Flux in the Northeast Atlantic. *Global*  
 790       *Biogeochemical Cycles*, 32(12), 1803–1814. doi: 10.1029/2018GB005963
- 791       Boyd, P. W., Claustre, H., Levy, M., Siegel, D. A., & Weber, T. (2019). Multi-  
 792       faceted particle pumps drive carbon sequestration in the ocean. *Nature*,  
 793       568(7752), 327. doi: 10.1038/s41586-019-1098-2
- 794       Brannigan, L. (2016). Intense submesoscale upwelling in anticyclonic eddies. *Geo-  
 795       physical Research Letters*, 43(7), 3360–3369. doi: 10.1002/2016GL067926
- 796       Briggs, N., Dall'Olmo, G., & Claustre, H. (2020). Major role of particle fragmen-  
 797       tation in regulating biological sequestration of CO<sub>2</sub> by the oceans. *Science*,  
 798       367(6479), 791–793. doi: 10.1126/science.aay1790
- 799       Briggs, N., Perry, M. J., Cetinić, I., Lee, C., D'Asaro, E., Gray, A. M., & Rehm, E.  
 800       (2011). High-resolution observations of aggregate flux during a sub-polar North  
 801       Atlantic spring bloom. *Deep Sea Research Part I: Oceanographic Research*  
 802       Papers, 58(10), 1031–1039. doi: 10.1016/j.dsr.2011.07.007
- 803       Buesseler, K. O., & Boyd, P. W. (2009). Shedding light on processes that con-  
 804       trol particle export and flux attenuation in the twilight zone of the open  
 805       ocean. *Limnology and Oceanography*, 54(4), 1210–1232. doi: 10.4319/  
 806       lo.2009.54.4.1210
- 807       Dall'Olmo, G., Dingle, J., Polimene, L., Brewin, R. J. W., & Claustre, H. (2016).  
 808       Substantial energy input to the mesopelagic ecosystem from the seasonal  
 809       mixed-layer pump. *Nature Geoscience*, 9(11), 820–823. doi: 10.1038/  
 810       ngeo2818
- 811       de Baar, H. J. W., de Jong, J. T. M., Nolting, R. F., Timmermans, K. R., van  
 812       Leeuwe, M. A., Bathmann, U., ... Sildam, J. (1999). Low dissolved Fe and  
 813       the absence of diatom blooms in remote Pacific waters of the Southern Ocean.  
 814       *Marine Chemistry*, 66(1), 1–34. doi: 10.1016/S0304-4203(99)00022-5
- 815       Dever, M., Nicholson, D., Omand, M., & Mahadevan, A. (2021). Size-differentiated  
 816       export flux in different dynamical regimes in the ocean. *Global Biogeochemical*  
 817       *Cycles*, 35(3), e2020GB006764.
- 818       Dong, S., Sprintall, J., Gille, S. T., & Talley, L. (2008). Southern Ocean mixed-  
 819       layer depth from Argo float profiles. *Journal of Geophysical Research: Oceans*,  
 820       113(C6). Retrieved 2021-04-01, from <https://agupubs.onlinelibrary.wiley.com/doi/abs/10.1029/2006JC004051> doi: <https://doi.org/10.1029/2006JC004051>
- 821       Dufour, C. O., Griffies, S. M., de Souza, G. F., Frenger, I., Morrison, A. K., Palter,  
 822       J. B., ... Slater, R. D. (2015). Role of Mesoscale Eddies in Cross-Frontal  
 823       Transport of Heat and Biogeochemical Tracers in the Southern Ocean. *Journal*  
 824       *of Physical Oceanography*, 45(12), 3057–3081. doi: 10.1175/JPO-D-14-0240.1
- 825       du Plessis, M., Swart, S., Ansorge, I. J., & Mahadevan, A. (2017). Subme-  
 826       soscale processes promote seasonal restratification in the Subantarctic  
 827       Ocean. *Journal of Geophysical Research: Oceans*, 122(4), 2960–2975. doi:  
 828       10.1002/2016JC012494
- 829       du Plessis, M., Swart, S., Ansorge, I. J., Mahadevan, A., & Thompson, A. F.  
 830       (2019). Southern Ocean Seasonal Restratification Delayed by Submesoscale  
 831       Wind-Front Interactions. *Journal of Physical Oceanography*, 49(4), 1035–1053.  
 832       doi: 10.1175/JPO-D-18-0136.1
- 833       Freeman, N. M., Lovenduski, N. S., Munro, D. R., Krumhardt, K. M., Lindsay, K.,  
 834       Long, M. C., & MacLennan, M. (2018). The Variable and Changing South-  
 835       ern Ocean Silicate Front: Insights From the CESM Large Ensemble. *Global*  
 836       *Biogeochemical Cycles*, 32(12), 1803–1814. doi: 10.1029/2018GB005963
- 837

- 838      *Biogeochemical Cycles*, 32(5), 752–768. doi: 10.1029/2017GB005816
- 839      Freilich, M. A., & Mahadevan, A. (2019). Decomposition of Vertical Velocity for  
840      Nutrient Transport in the Upper Ocean. *Journal of Physical Oceanography*,  
841      49(6), 1561–1575. doi: 10.1175/JPO-D-19-0002.1
- 842      Frölicher, T. L., Sarmiento, J. L., Paynter, D. J., Dunne, J. P., Krasting, J. P., &  
843      Winton, M. (2015). Dominance of the Southern Ocean in Anthropogenic Car-  
844      bon and Heat Uptake in CMIP5 Models. *Journal of Climate*, 28(2), 862–886.  
845      doi: 10.1175/JCLI-D-14-00117.1
- 846      Giddy, I., Swart, S., du Plessis, M., Thompson, A. F., & Nicholson, S.-A. (2021).  
847      Stirring of Sea-Ice Meltwater Enhances Submesoscale Fronts in the Southern  
848      Ocean. *Journal of Geophysical Research: Oceans*, 126(4), e2020JC016814. Re-  
849      trieved 2021-04-01, from <https://agupubs.onlinelibrary.wiley.com/doi/abs/10.1029/2020JC016814> doi: <https://doi.org/10.1029/2020JC016814>
- 850      Gille, S. T., & Kelly, K. A. (1996). Scales of spatial and temporal variability in  
851      the Southern Ocean. *Journal of Geophysical Research: Oceans*, 101(C4), 8759–  
852      8773. doi: 10.1029/96JC00203
- 853      Gray, A. R., Johnson, K. S., Bushinsky, S. M., Riser, S. C., Russell, J. L., Tal-  
854      ley, L. D., ... Sarmiento, J. L. (2018). Autonomous Biogeochemical  
855      Floats Detect Significant Carbon Dioxide Outgassing in the High-Latitude  
856      Southern Ocean. *Geophysical Research Letters*, 45(17), 9049–9057. doi:  
857      10.1029/2018GL078013
- 858      Gruber, N., Landschützer, P., & Lovenduski, N. S. (2019). The Variable Southern  
859      Ocean Carbon Sink. *Annual Review of Marine Science*, 11(1), 159–186. doi:  
860      10.1146/annurev-marine-121916-063407
- 861      Hantjens, N., Boss, E., & Talley, L. D. (2017). Revisiting Ocean Color al-  
862      gorithms for chlorophyll a and particulate organic carbon in the South-  
863      ern Ocean using biogeochemical floats. *Journal of Geophysical Re-*  
864      *search: Oceans*, 122(8), 6583–6593. Retrieved 2021-05-17, from <http://agupubs.onlinelibrary.wiley.com/doi/abs/10.1002/2017JC012844> doi:  
865      <https://doi.org/10.1002/2017JC012844>
- 866      Johnson, K. S., Coletti, L. J., Jannasch, H. W., Sakamoto, C. M., Swift, D. D.,  
867      & Riser, S. C. (2013, August). Long-Term Nitrate Measurements in the  
868      Ocean Using the in situ Ultraviolet Spectrophotometer: Sensor Integration  
869      into the APEX Profiling Float. *Journal of Atmospheric and Oceanic Tech-*  
870      *nology*, 30(8), 1854–1866. Retrieved 2021-05-17, from [https://journals.ametsoc.org/view/journals/atot/30/8/jtech-d-12-00221\\_1.xml](https://journals.ametsoc.org/view/journals/atot/30/8/jtech-d-12-00221_1.xml) doi:  
871      10.1175/JTECH-D-12-00221.1
- 872      Johnson, K. S., Jannasch, H. W., Coletti, L. J., Elrod, V. A., Martz, T. R.,  
873      Takeshita, Y., ... Connery, J. G. (2016, March). Deep-Sea DuraFET: A  
874      Pressure Tolerant pH Sensor Designed for Global Sensor Networks. *Analytical  
875      Chemistry*, 88(6), 3249–3256. Retrieved 2021-05-17, from <https://doi.org/10.1021/acs.analchem.5b04653> doi: 10.1021/acs.analchem.5b04653
- 876      Johnson, K. S., Plant, J. N., Coletti, L. J., Jannasch, H. W., Sakamoto, C. M.,  
877      Riser, S. C., ... Sarmiento, J. L. (2017). Biogeochemical sensor performance in  
878      the SOCCOM profiling float array. *Journal of Geophysical Research: Oceans*,  
879      122(8), 6416–6436. doi: 10.1002/2017JC012838
- 880      Johnson, K. S., Plant, J. N., Riser, S. C., & Gilbert, D. (2015). Air Oxygen Cali-  
881      bration of Oxygen Optodes on a Profiling Float Array. *Journal of Atmospheric  
882      and Oceanic Technology*, 32(11), 2160–2172. doi: 10.1175/JTECH-D-15-0101  
883      .1
- 884      Joyce, T. M., Zenk, W., & Toole, J. M. (1978). The anatomy of the Antarctic Polar  
885      Front in the Drake Passage. *J. Geophys. Res.*, 83, 6093–6113.
- 886      Kim, Y. S., & Orsi, A. H. (2014). On the Variability of Antarctic Circumpolar Cur-  
887      rent Fronts Inferred from 1992–2011 Altimetry. *Journal of Physical Oceanogra-*  
888      *phy*, 44(12), 3054–3071. doi: 10.1175/JPO-D-13-0217.1

- 893 Klein, P., & Lapeyre, G. (2009). The Oceanic Vertical Pump Induced by Mesoscale  
 894 and Submesoscale Turbulence. *Annual Review of Marine Science*, 1(1), 351–  
 895 375. doi: 10.1146/annurev.marine.010908.163704
- 896 Kostadinov, T. S., Siegel, D. A., & Maritorena, S. (2009). Retrieval of the particle  
 897 size distribution from satellite ocean color observations. *Journal of Geophysical  
 898 Research: Oceans*, 114(C9). doi: 10.1029/2009JC005303
- 899 Levy, M., Bopp, L., Karleskind, P., Resplandy, L., Ethe, C., & Pinsard, F. (2013).  
 900 Physical pathways for carbon transfers between the surface mixed layer and  
 901 the ocean interior. *Global Biogeochemical Cycles*, 27(4), 1001–1012. doi:  
 902 10.1002/gbc.20092
- 903 Lévy, M., Ferrari, R., Franks, P. J. S., Martin, A. P., & Rivière, P. (2012). Bringing  
 904 physics to life at the submesoscale. *Geophysical Research Letters*, 39(14). doi:  
 905 10.1029/2012GL052756
- 906 Lévy, M., Franks, P. J. S., & Smith, K. S. (2018). The role of submesoscale currents  
 907 in structuring marine ecosystems. *Nature Communications*, 9(1), 4758. doi: 10  
 908 .1038/s41467-018-07059-3
- 909 Llort, J., Langlais, C., Matear, R., Moreau, S., Lenton, A., & Strutton, P. G. (2018).  
 910 Evaluating Southern Ocean Carbon Eddy-Pump From Biogeochemical-Argo  
 911 Floats. *Journal of Geophysical Research: Oceans*, 123(2), 971–984. doi:  
 912 10.1002/2017JC012861
- 913 Loisel, H., Nicolas, J.-M., Sciandra, A., Stramski, D., & Poteau, A. (2006). Spec-  
 914 tral dependency of optical backscattering by marine particles from satellite  
 915 remote sensing of the global ocean. *Journal of Geophysical Research: Oceans*,  
 916 111(C9). doi: 10.1029/2005JC003367
- 917 Lu, J., & Speer, K. (2010). Topography, jets and eddy mixing in the Southern  
 918 Ocean. *J. Mar. Res.*, 68, 479–502.
- 919 Lu, J., Wang, F., Liu, H., & Lin, P. (2016). Stationary mesoscale eddies, upgradient  
 920 eddy fluxes, and the anisotropy of eddy diffusivity. *Geophysical Research Let-  
 921 ters*, 43(2), 743–751. doi: <https://doi.org/10.1002/2015GL067384>
- 922 MacCready, P., & Rhines, P. B. (2001). Meridional transport across a zonal channel:  
 923 Topographic localization. *J. Phys. Oceanogr.*, 31, 1427–1439.
- 924 Mahadevan, A. (2016). The Impact of Submesoscale Physics on Primary Produc-  
 925 tivity of Plankton. *Annual Review of Marine Science*, 8(1), 161–184. doi: 10  
 926 .1146/annurev-marine-010814-015912
- 927 Marshall, J., & Speer, K. (2012). Closure of the meridional overturning circulation  
 928 through Southern Ocean upwelling. *Nature Geoscience*, 5(3), 171–180. doi: 10  
 929 .1038/ngeo1391
- 930 Mazloff, M. R., Cornuelle, B. D., Gille, S. T., & Verdy, A. (2018). Correlation  
 931 Lengths for Estimating the Large-Scale Carbon and Heat Content of the  
 932 Southern Ocean. *Journal of Geophysical Research: Oceans*, 123(2), 883–  
 933 901. Retrieved 2021-03-30, from <https://agupubs.onlinelibrary.wiley.com/doi/abs/10.1002/2017JC013408> doi: <https://doi.org/10.1002/2017JC013408>
- 934 McDougall, T. J., & Barker, P. M. (2011). Getting started with teos-10 and the  
 935 gibbs seawater (gsw) oceanographic toolbox. *SCOR/IAPSO WG*, 127, 1–28.
- 936 McWilliams, J. C. (2016). Submesoscale currents in the ocean. *Proceedings of the  
 937 Royal Society A: Mathematical, Physical and Engineering Sciences*, 472(2189),  
 938 20160117. doi: 10.1098/rspa.2016.0117
- 939 Meredith, M. P., Schofield, O., Newman, L., Urban, E., & Sparrow, M. (2013). The  
 940 vision for a Southern Ocean Observing System. *Curr. Op. Env. Sust.*, 5, 306–  
 941 313.
- 942 Naveira Garabato, A. C., Ferrari, R., & Polzin, K. L. (2011). Eddy stirring in the  
 943 Southern Ocean. *J. Geophys. Res.*, 116, C09019.
- 944 Omand, M. M., D'Asaro, E. A., Lee, C. M., Perry, M. J., Briggs, N., Cetinić, I.,  
 945 & Mahadevan, A. (2015). Eddy-driven subduction exports particulate or-

- 948 ganic carbon from the spring bloom. *Science*, 348(6231), 222–225. doi:  
 949 10.1126/science.1260062
- 950 Orsi, A. H., Whitworth, T., & Nowlin, W. D. (1995). On the meridional extent  
 951 and fronts of the Antarctic Circumpolar Current. *Deep Sea Research Part I: Oceanographic Research Papers*, 42(5), 641–673. doi: 10.1016/0967-0637(95)00021-W
- 952 Palevsky, H. I., Quay, P. D., Lockwood, D. E., & Nicholson, D. P. (2016). The annual  
 953 cycle of gross primary production, net community production, and export efficiency across the North Pacific Ocean. *Global Biogeochemical Cycles*, 30(2),  
 954 361–380. doi: 10.1002/2015GB005318
- 955 Pollard, R. T., & Read, J. F. (2001). Circulation pathways and transports of the  
 956 Southern Ocean in the vicinity of the Southwest Indian Ridge. *J. Geophys. Res.*, 106, 2881–2898.
- 957 Rintoul, S. R. (2018). The global influence of localized dynamics in the Southern  
 958 Ocean. *Nature*, 558(7709), 209–218. doi: 10.1038/s41586-018-0182-3
- 959 Rintoul, S. R., & Naveira Garabato, A. C. (2013). Chapter 18 - Dynamics of  
 960 the Southern Ocean Circulation. In G. Siedler, S. M. Griffies, J. Gould, &  
 961 J. A. Church (Eds.), *International Geophysics* (Vol. 103, pp. 471–492). doi:  
 962 10.1016/B978-0-12-391851-2.00018-0
- 963 Riser, S. C., Freeland, H. J., Roemmich, D., Wijffels, S., Troisi, A., Belbéoch, M., ...  
 964 Jayne, S. R. (2016). Fifteen years of ocean observations with the global Argo  
 965 array. *Nature Climate Change*, 6(2), 145–153. doi: 10.1038/nclimate2872
- 966 Roach, C. J., Balwada, D., & Speer, K. (2016). Horizontal mixing in the Southern  
 967 Ocean from Argo float trajectories. *Journal of Geophysical Research: Oceans*,  
 968 121(8), 5570–5586. doi: <https://doi.org/10.1002/2015JC011440>
- 969 Roemmich, D., & Gilson, J. (2009). The 20042008 mean and annual cycle of temperature,  
 970 salinity, and steric height in the global ocean from the Argo Program.  
 971 *Progress in Oceanography*, 82(2), 81–100. doi: 10.1016/j.pocean.2009.03.004
- 972 Rosso, I., Hogg, A. M., Kiss, A. E., & Gayen, B. (2015). Topographic influence on  
 973 submesoscale dynamics in the Southern Ocean. *Geophysical Research Letters*,  
 974 42(4), 1139–1147. doi: 10.1002/2014GL062720
- 975 Rosso, I., Hogg, A. M., Strutton, P. G., Kiss, A. E., Matear, R., Klocker, A., & van  
 976 Sebille, E. (2014). Vertical transport in the ocean due to sub-mesoscale structures:  
 977 Impacts in the Kerguelen region. *Ocean Modelling*, 80, 10–23. doi:  
 978 10.1016/j.ocemod.2014.05.001
- 979 Rousseaux, C. S., & Gregg, W. W. (2014). Interannual Variation in Phytoplankton  
 980 Primary Production at A Global Scale. *Remote Sensing*, 6(1), 1–19. doi: 10  
 981 .3390/rs6010001
- 982 Ruiz, S., Pascual, A., Garau, B., Pujol, I., & Tintoré, J. (2009). Vertical motion in  
 983 the upper ocean from glider and altimetry data. *Geophysical Research Letters*,  
 984 36(14). doi: 10.1029/2009GL038569
- 985 Sallée, J.-B., Matear, R. J., Rintoul, S. R., & Lenton, A. (2012). Localized subduction  
 986 of anthropogenic carbon dioxide in the Southern Hemisphere oceans. *Nature  
 987 Geoscience*, 5(8), 579–584. doi: 10.1038/ngeo1523
- 988 Schlitzer, R. (2002). Carbon export fluxes in the Southern Ocean: results from  
 989 inverse modeling and comparison with satellite-based estimates. *Deep Sea  
 990 Research Part II: Topical Studies in Oceanography*, 49(9), 1623–1644. doi:  
 991 10.1016/S0967-0645(02)00004-8
- 992 Siegelman, L. (2020). Energetic Submesoscale Dynamics in the Ocean Interior. *Journal  
 993 of Physical Oceanography*, 50(3), 727–749. doi: 10.1175/JPO-D-19-0253.1
- 994 Siegelman, L., Klein, P., Rivière, P., Thompson, A. F., Torres, H. S., Flexas,  
 995 M., & Menemenlis, D. (2020). Enhanced upward heat transport at  
 996 deep submesoscale ocean fronts. *Nature Geoscience*, 13(1), 50–55. doi:  
 997 10.1038/s41561-019-0489-1
- 998 Siegelman, L., O'Toole, M., Flexas, M., Rivière, P., & Klein, P. (2019). Subme-

- 1003            soscale ocean fronts act as biological hotspot for southern elephant seal. *Scientific Reports*, 9(1), 1–13. doi: 10.1038/s41598-019-42117-w
- 1004            Smith, K. S., & Ferrari, R. (2009). The Production and Dissipation of Compensated  
1005            Thermohaline Variance by Mesoscale Stirring. *Journal of Physical Oceanography*, 39(10),  
1006            2477–2501. doi: 10.1175/2009JPO4103.1
- 1007            Sokolov, S., & Rintoul, S. R. (2009). Circumpolar structure and distribution of  
1008            the Antarctic Circumpolar Current fronts: 1. Mean circumpolar paths. *Journal of Geophysical Research: Oceans*, 114(C11). doi: <https://doi.org/10.1029/2008JC005108>
- 1009            Stewart, K. D., & Haine, T. W. N. (2016). Thermobaricity in the Transition Zones  
1010            between Alpha and Beta Oceans. *Journal of Physical Oceanography*, 46(6),  
1011            1805–1821. doi: 10.1175/JPO-D-16-0017.1
- 1012            Stukel, M. R., Aluwihare, L. I., Barbeau, K. A., Chekalyuk, A. M., Goericke,  
1013            R., Miller, A. J., ... Landry, M. R. (2017). Mesoscale ocean fronts en-  
1014            hance carbon export due to gravitational sinking and subduction. *Proceedings of the National Academy of Sciences*, 114(6), 1252–1257. doi:  
1015            10.1073/pnas.1609435114
- 1016            Stukel, M. R., & Ducklow, H. W. (2017). Stirring Up the Biological Pump: Vertical  
1017            Mixing and Carbon Export in the Southern Ocean. *Global Biogeochemical Cycles*, 31(9),  
1018            1420–1434. doi: 10.1002/2017GB005652
- 1019            Su, Z., Wang, J., Klein, P., Thompson, A. F., & Menemenlis, D. (2018). Ocean sub-  
1020            mesoscales as a key component of the global heat budget. *Nature Communications*, 9(1),  
1021            775. doi: 10.1038/s41467-018-02983-w
- 1022            Sutton, A. J., Williams, N. L., & Tilbrook, B. (2021). Constraining  
1023            Southern Ocean CO<sub>2</sub> Flux Uncertainty Using Uncrewed Sur-  
1024            face Vehicle Observations. *Geophysical Research Letters*, 48(3),  
1025            e2020GL091748. Retrieved 2021-03-30, from <https://agupubs.onlinelibrary.wiley.com/doi/abs/10.1029/2020GL091748> (eprint:  
1026            <https://agupubs.onlinelibrary.wiley.com/doi/pdf/10.1029/2020GL091748>) doi:  
1027            <https://doi.org/10.1029/2020GL091748>
- 1028            Swart, S., Plessis, M. D. d., Thompson, A. F., Biddle, L. C., Giddy, I., Linders, T.,  
1029            ... Nicholson, S.-A. (2020). Submesoscale Fronts in the Antarctic Marginal  
1030            Ice Zone and Their Response to Wind Forcing. *Geophysical Research Letters*,  
1031            47(6), e2019GL086649. doi: <https://doi.org/10.1029/2019GL086649>
- 1032            Tamsitt, V., Drake, H. F., Morrison, A. K., Talley, L. D., Dufour, C. O., Gray,  
1033            A. R., ... Weijer, W. (2017). Spiraling pathways of global deep waters to  
1034            the surface of the Southern Ocean. *Nature Communications*, 8(1), 1–10. doi:  
1035            10.1038/s41467-017-00197-0
- 1036            Tengberg, A., Hovdenes, J., Andersson, H. J., Brocandel, O., Diaz, R., Hebert, D.,  
1037            ... Stangelmayer, A. (2006). Evaluation of a lifetime-based optode to measure  
1038            oxygen in aquatic systems. *Limnology and Oceanography: Methods*, 4(2), 7–17.  
1039            Retrieved 2021-05-17, from <https://aslopubs.onlinelibrary.wiley.com/doi/abs/10.4319/lom.2006.4.7> doi: <https://doi.org/10.4319/lom.2006.4.7>
- 1040            Thomas, L. N., & Lee, C. M. (2005). Intensification of Ocean Fronts by Down-Front  
1041            Winds. *Journal of Physical Oceanography*, 35(6), 1086–1102. doi: 10.1175/  
1042            JPO2737.1
- 1043            Thomas, L. N., Tandon, A., & Mahadevan, A. (2008). Submesoscale processes and  
1044            dynamics. *Washington DC American Geophysical Union Geophysical Mono-*  
1045            *graph Series*, 177, 17–38. doi: 10.1029/177GM04
- 1046            Thompson, A. F., Lazar, A., Buckingham, C., Naveira Garabato, A. C., Damerell,  
1047            G. M., & Heywood, K. J. (2016). Open-Ocean Submesoscale Motions: A Full  
1048            Seasonal Cycle of Mixed Layer Instabilities from Gliders. *Journal of Physical  
1049            Oceanography*, 46(4), 1285–1307. doi: 10.1175/JPO-D-15-0170.1
- 1050            Thompson, A. F., & Naveira Garabato, A. C. (2014). Equilibration of the Antarc-  
1051            tic Circumpolar Current by Standing Meanders. *Journal of Physical Oceanog-*

**Figure 1.** Standing meander location. (a) Bathymetry of the western Indian sector of the Southern Ocean. The white dotted line shows the path of the I6S GO-SHIP cruise track; the red box outlines the study region shown in panel (b). Thin black lines denote the major fronts of the ACC as defined in Gray et al. (2018). Southwest Indian Ridge is labeled as SWIR. (b) Latitude of the SSH contour corresponding to the PF as defined by Kim and Orsi (2014). Gray lines show weekly examples from 2017–2020, and the black line shows the mean location. Purple lines show examples of the PF location from every 3 days during the glider deployment timeframe (April 29–July 25, 2019). Blue and red lines are the maximum and minimum latitudinal extents of the PF, respectively.

- raphy, 44(7), 1811–1828. doi: 10.1175/JPO-D-13-0163.1
- Thompson, A. F., & Sallée, J.-B. (2012). Jets and Topography: Jet Transitions and the Impact on Transport in the Antarctic Circumpolar Current. *Journal of Physical Oceanography*, 42(6), 956–972. doi: 10.1175/JPO-D-11-0135.1
- Uchida, T., Balwada, D., Abernathey, R., McKinley, G., Smith, S., & Lévy, M. (2019). The Contribution of Submesoscale over Mesoscale Eddy Iron Transport in the Open Southern Ocean. *Journal of Advances in Modeling Earth Systems*, 11(12), 3934–3958. doi: 10.1029/2019MS001805
- Vaillancourt, R. D., Brown, C. W., Guillard, R. R. L., & Balch, W. M. (2004). Light backscattering properties of marine phytoplankton: relationships to cell size, chemical composition and taxonomy. *Journal of Plankton Research*, 26(2), 191–212. doi: 10.1093/plankt/fbh012
- Viglione, G. A., & Thompson, A. F. (2016). Lagrangian pathways of upwelling in the Southern Ocean. *Journal of Geophysical Research: Oceans*, 121(8), 6295–6309. doi: <https://doi.org/10.1002/2016JC011773>
- Viglione, G. A., Thompson, A. F., Flexas, M. M., Sprintall, J., & Swart, S. (2018). Abrupt Transitions in Submesoscale Structure in Southern Drake Passage: Glider Observations and Model Results. *Journal of Physical Oceanography*, 48(9), 2011–2027. doi: 10.1175/JPO-D-17-0192.1
- Wei, Y., Gille, S. T., Mazloff, M. R., Tamsitt, V., Swart, S., Chen, D., & Newman, L. (2020, August). Optimizing Mooring Placement to Constrain Southern Ocean AirSea Fluxes. *Journal of Atmospheric and Oceanic Technology*, 37(8), 1365–1385. Retrieved 2021-03-30, from <https://journals.ametsoc.org/view/journals/atot/37/8/jtechD190203.xml> doi: 10.1175/JTECH-D-19-0203.1
- Witter, D. L., & Chelton, D. B. (1998). Eddy–mean flow interaction in zonal oceanic jet flow along zonal ridge topography. *J. Phys. Oceanogr.*, 28, 2019–2039.
- Youngs, M. K., Thompson, A. F., Lazar, A., & Richards, K. J. (2017). ACC Meanders, Energy Transfer, and Mixed Barotropic–Baroclinic Instability. *Journal of Physical Oceanography*, 47(6), 1291–1305. doi: 10.1175/JPO-D-16-0160.1
- Zhang, X., Hu, L., & He, M.-X. (2009, March). Scattering by pure seawater: Effect of salinity. *Optics Express*, 17(7), 5698–5710. doi: 10.1364/OE.17.005698

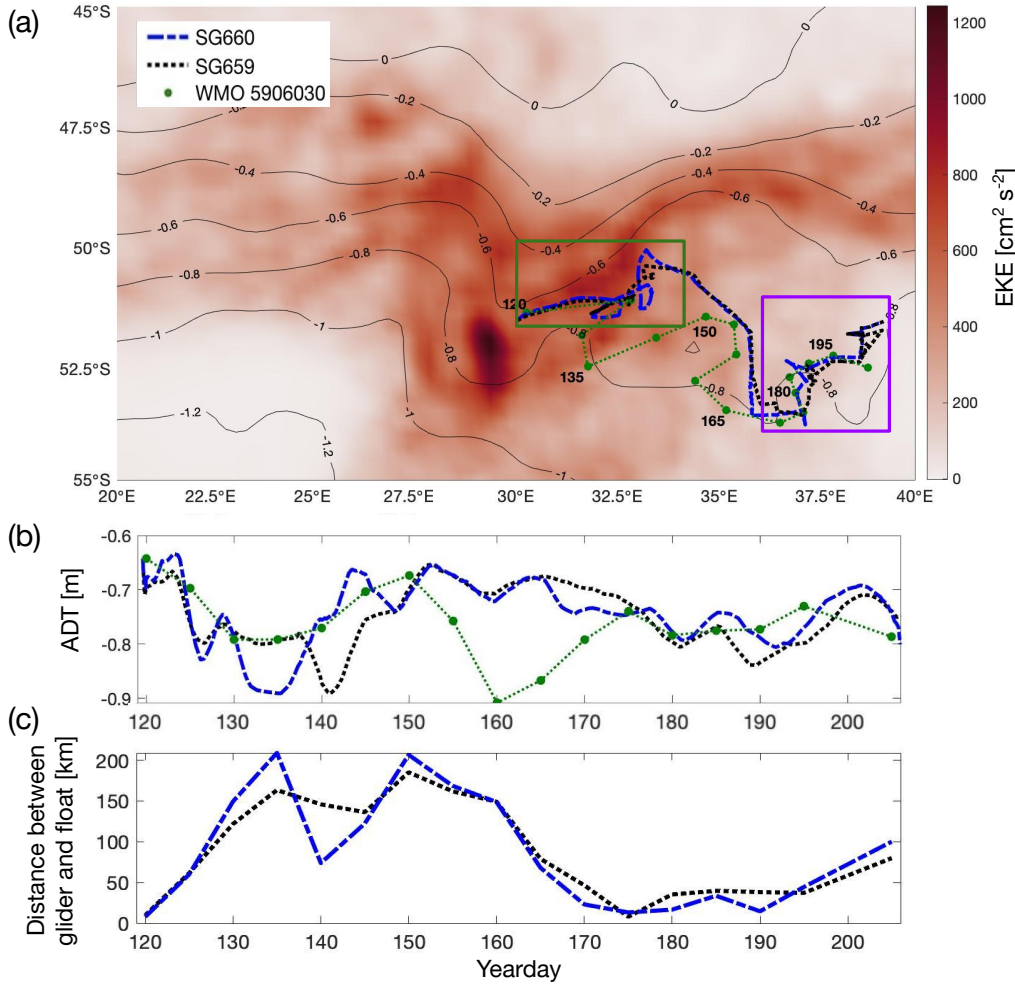


**Figure 2.** Study region: (a) Mean eddy kinetic energy (EKE;  $\text{cm}^2 \text{s}^{-2}$ ) from 2017-2020 in the same area as boxed in Figure 1a. Gray contours give the mean absolute dynamic topography (ADT) from AVISO over the same time period, ranging from -1.2 to 0 m with 0.2 m increments. Lines represent the paths of SG660 (blue) and SG659 (black) and the profile positions of float WMO 5906030 are denoted by green points. Numbers represent the yearday when the float performed a vertical profile. Green box represents the high-EKE region and purple box represents the low-EKE region as discussed in the text. (b) ADT values at the locations of the float and glider profiles. Although the gliders were persistently north of the float during the early stages of the deployment, they sampled similar water masses as indicated by their proximity in SSH space. (c) Distance [km] between each of the two gliders and the float.

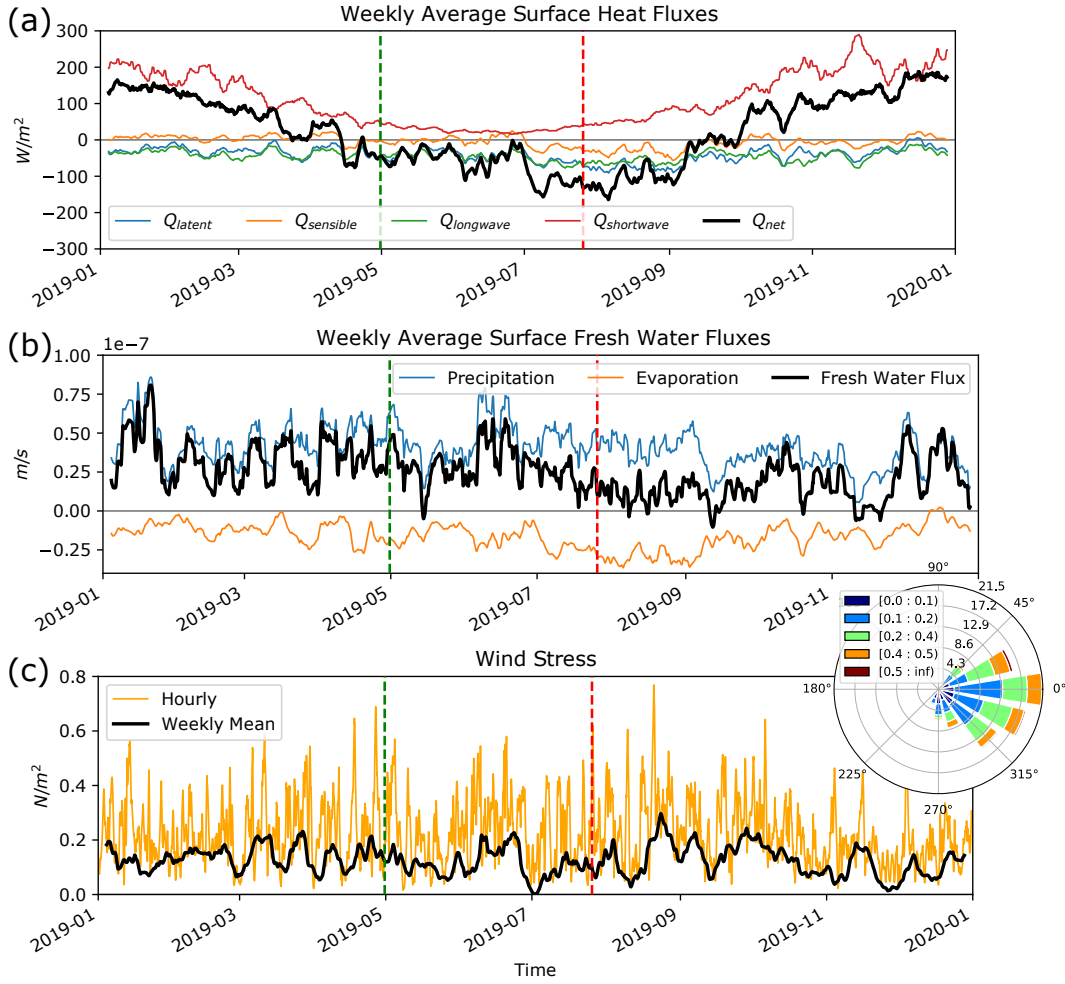


**Figure 3.** Surface forcing fields from ERA5: (a) Weekly-averaged surface heat fluxes ( $\text{W m}^{-2}$ ) and its components, (b) weekly-averaged surface freshwater fluxes ( $\text{m s}^{-1}$ ), and (c) hourly- and weekly-averaged surface wind stress ( $\text{N m}^{-2}$ ). All variables were averaged spatially over  $30 - 39^\circ\text{E}$  and  $50 - 53.5^\circ\text{S}$ . The inset (d) shows a windrose plot of the hourly wind stress during the period of glider deployment. The direction shows wind stress orientation while the legend indicates wind stress magnitude. The dashed vertical green and red lines in each panel represent the start and end dates of the glider surveys.

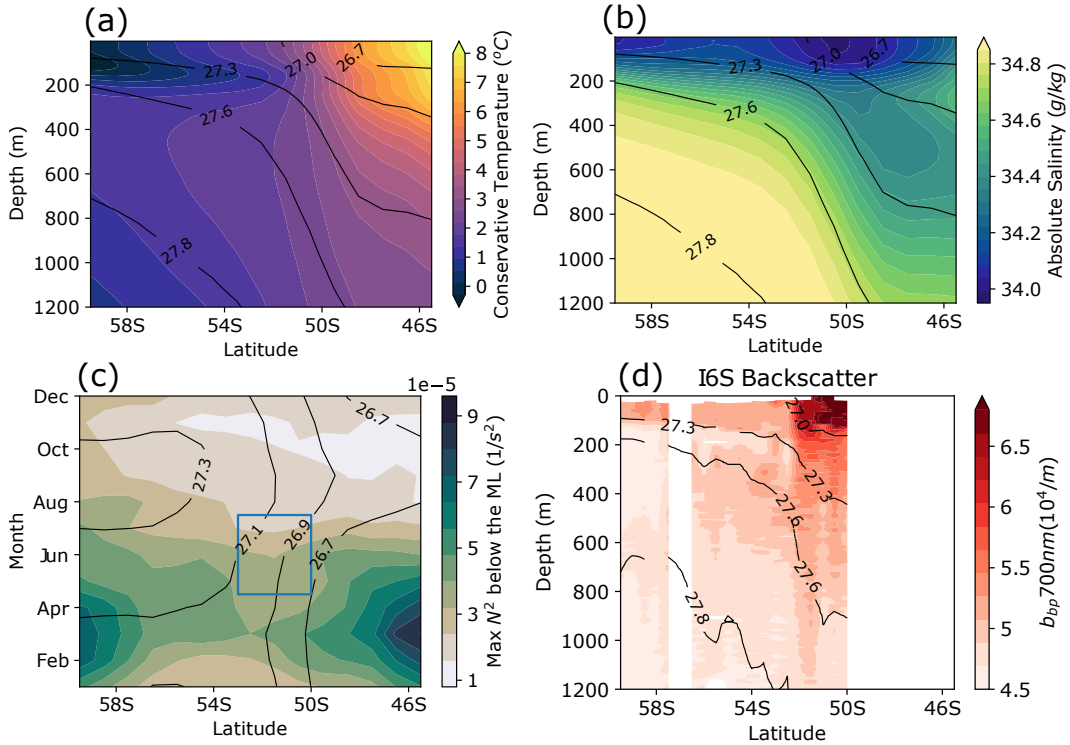


**Figure 4.** Hydrographic properties at 30°E. Depth vs latitude plots of (a) conservative temperature (°C) and (b) absolute salinity ( $\text{g kg}^{-1}$ ) at 30E from the Roemmich and Gilson (2009) climatological mean. (c) Hovmoller plot of the maximum  $N^2$  observed below the base of the mixed layer (ML), with the time and meridional extent of the glider sampling shown by the blue box, also from Roemmich and Gilson (2009). (d) Depth-latitude plot of de-spiked backscatter data collected during I06S (2019); note the different latitude axis range in this panel. The  $\sigma_0$  surfaces are shown as black contours, with panel (c) showing contours of surface  $\sigma_0$ . White space in panel (d) denotes a lack of data.

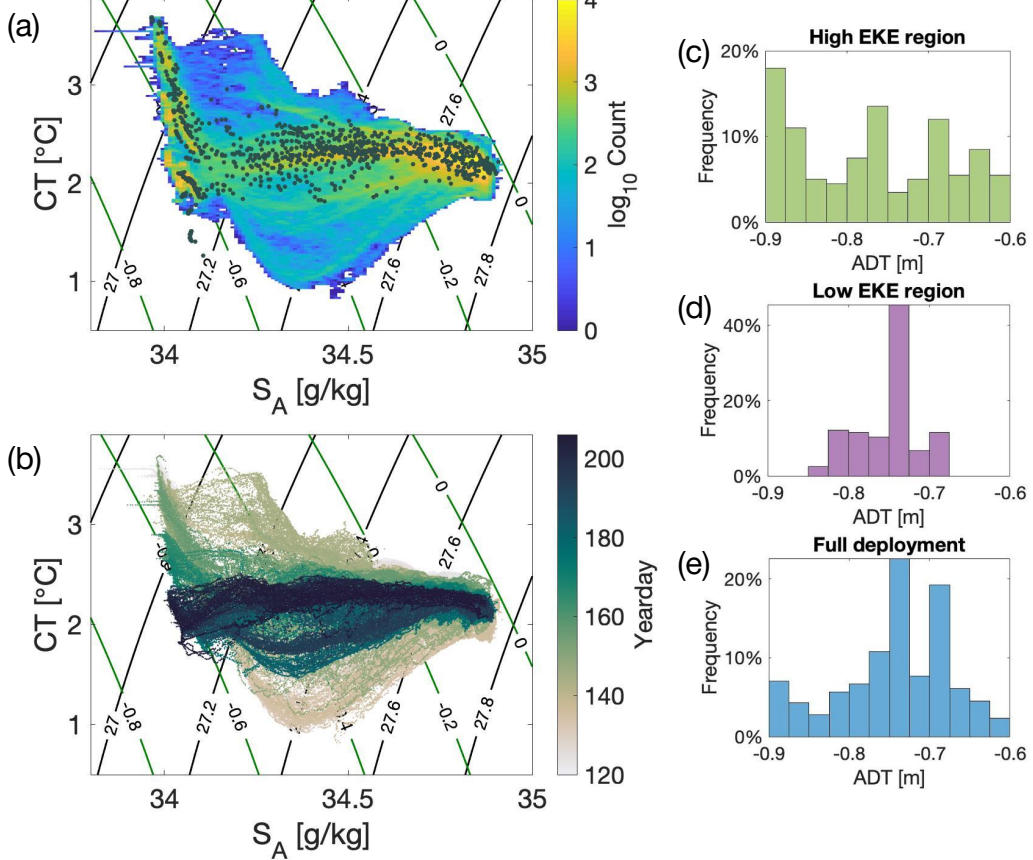


**Figure 5.** (a) Conservative temperature-Absolute salinity diagram for all observing platforms over the full deployment colored by the frequency of observations collected by the two gliders with given CT-SA properties, using discretizations of  $\Delta T = 0.02^\circ\text{C}$  and  $\Delta S = 0.01 \text{ g kg}^{-1}$ . Gray points are from the BGC-Argo float during the period April 29 - July 25, 2019. (b) Conservative temperature-Absolute salinity diagram colored by the yearday of the observation made by the two gliders. Black contours show potential density [ $\text{kg m}^{-3}$ ] referenced to the surface, and green contours show spice [ $\text{kg m}^{-3}$ ] referenced to the surface. Histograms of the absolute dynamic topography [m] (sea surface height) along the path of the gliders in (c) the high-EKE region (yearday 120-155), (d) the low-EKE region (yearday 170-206), and (e) the full deployment. Made from the joint data of SG659 and SG660.

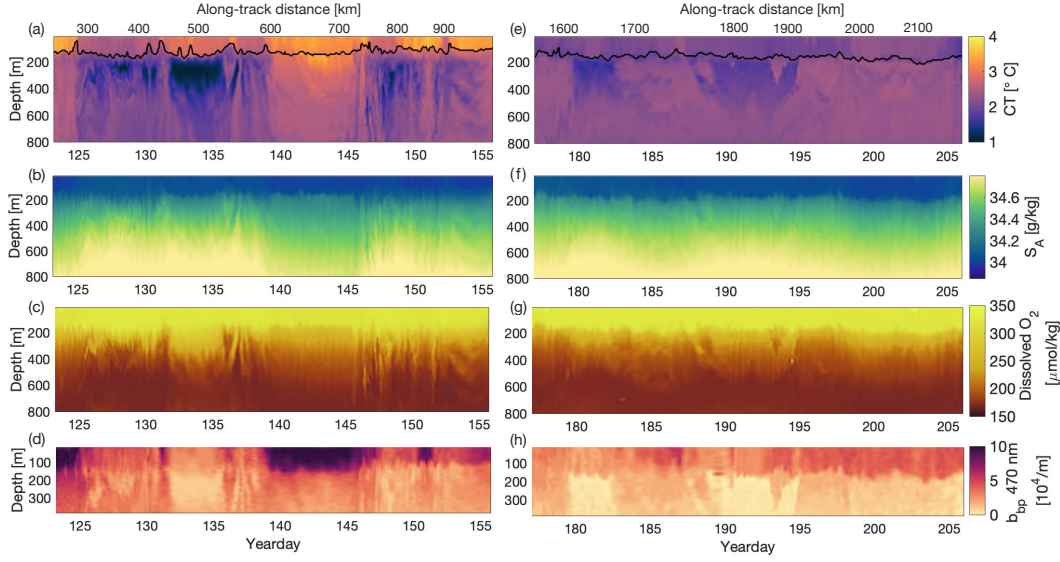


**Figure 6.** Glider tracer sections from SG660 in high-EKE region (yeardays 125-155) showing (a) conservative temperature [ $^{\circ}\text{C}$ ], (b) absolute salinity [ $\text{g kg}^{-1}$ ], (c) dissolved oxygen [ $\mu\text{mol kg}^{-1}$ ], and (d) backscatter at 470 nm [ $10^4 \text{ m}^{-1}$ ]. (e-h) Same as in panels (a-d) but for low-EKE region (yeardays 177-206). Black line in panels (a) and (e) designates the mixed layer depth. Color bars apply to both left-hand and right-hand panels. Note change in depth axis for (d) and (h) compared to the other panels.

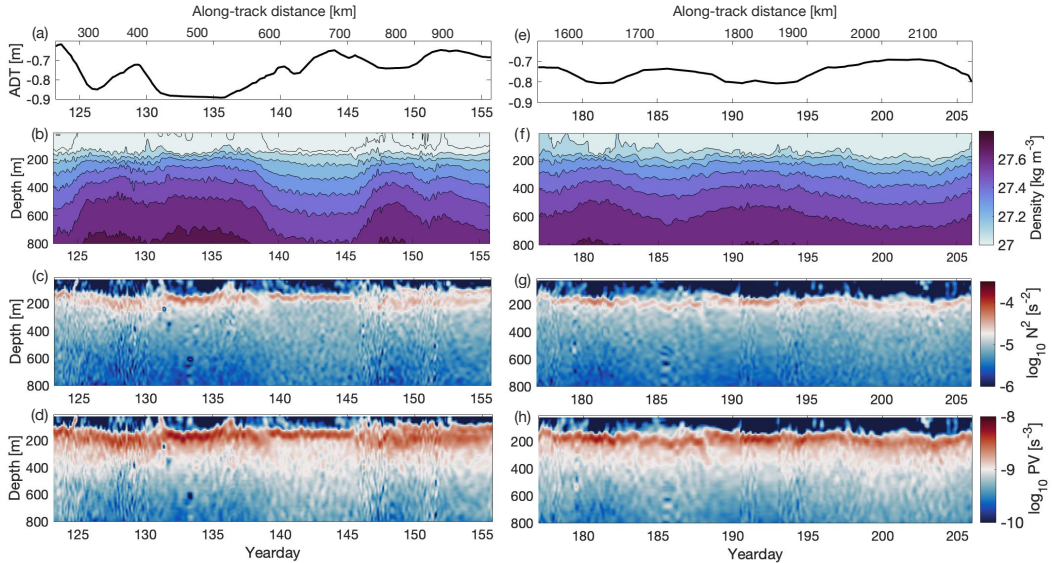


**Figure 7.** Glider derived tracer sections from SG660 in high-EKE region (yeardays 125-155) showing (a) absolute dynamic topography [m], (b) potential density [ $\text{kg m}^{-3}$ ], (c) vertical buoyancy gradient,  $N^2$  [ $\text{s}^{-2}$ ], and (d) Ertel Potential Vorticity (PV) [ $\text{s}^{-3}$ ]. (e-h) Same as in panels (a-d) but for low-EKE region (yeardays 177-206). Color bars apply to both left-hand and right-hand panels.

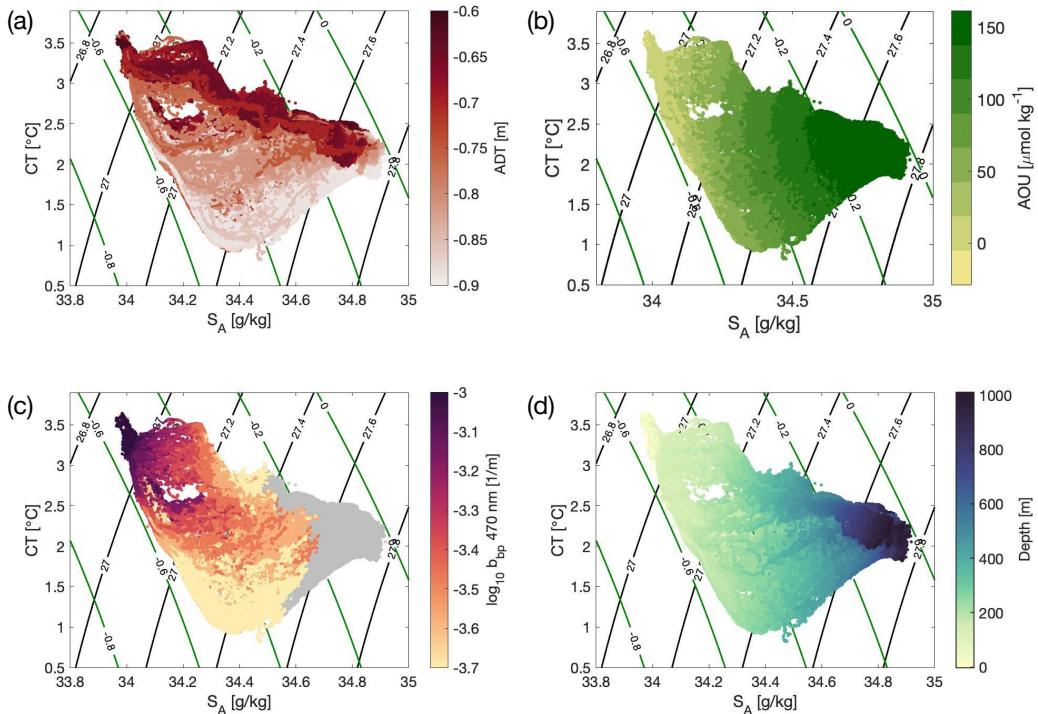


**Figure 8.** Distribution of physical and biogeochemical properties in temperature-salinity space from the standing meander region (yeardays 120–155). (a) Absolute dynamic topography (SSH) [m] for each glider profile, (b) apparent oxygen utilization (AOU) [ $\mu \text{ mol kg}^{-1}$ ], (c)  $\log_{10} b_{bp}$  at 470 nm [ $m^{-1}$ ], and (d) depth [m]. Gray points in the backscatter plot represent data between 400–1000 m where temperature, salinity, and oxygen measurements were collected but biogeochemical properties were not. In all panels, black contours show potential density [ $\text{kg m}^{-3}$ ] referenced to the surface, and green contours show sigma [ $\text{kg m}^{-3}$ ] referenced to the surface. Made from the joint data of SG659 and SG660.

Accepted Article

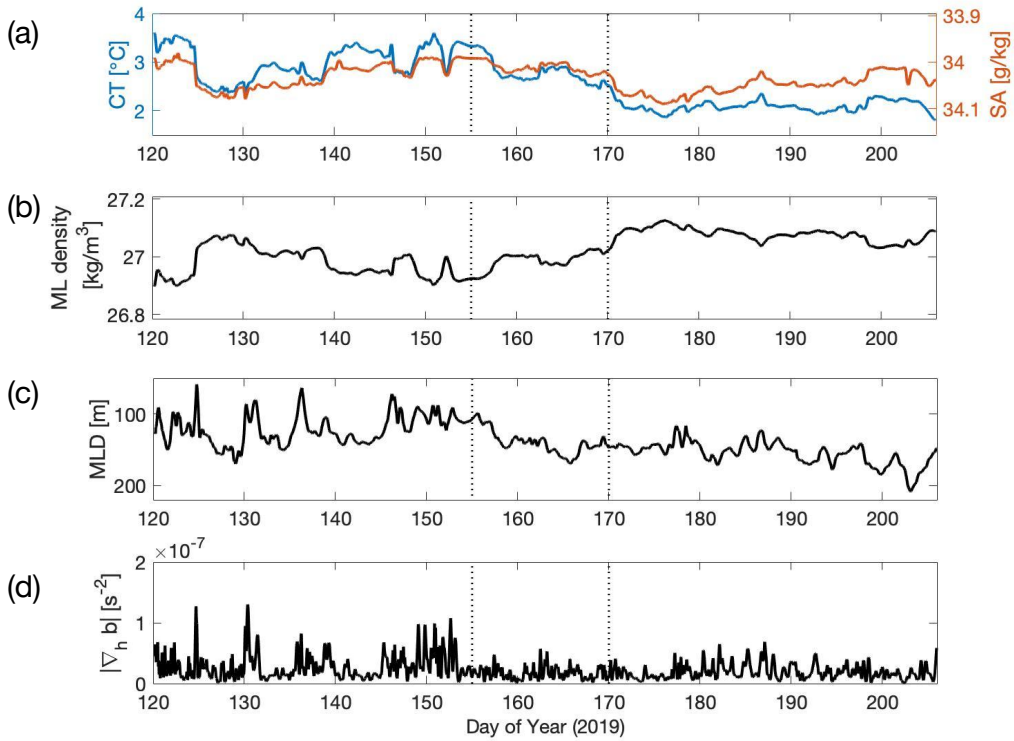


**Figure 9.** (a) Mixed layer temperature (blue line) and salinity (red line) variations throughout the glider time series. The vertical axes are scaled by  $\alpha$  (temperature) and  $\beta$  (salinity) so that variations in CT and  $S_A$  have equal effects on density. (b) Mixed layer density [ $\text{kg m}^{-3}$ ]. Vertical axis has been scaled to the minimum and maximum contributions by the temperature and salinity presented in panel (a). (c) MLD as defined by a density difference criteria of  $0.05 \text{ kg m}^{-3}$  from a 10-m reference level. (d) Horizontal gradient of buoyancy in the mixed layer. Dotted line at yearday 155 denotes an end to the high-EKE region and the dotted line at yearday 170 denotes the start of the low-EKE region. Data from SG660.

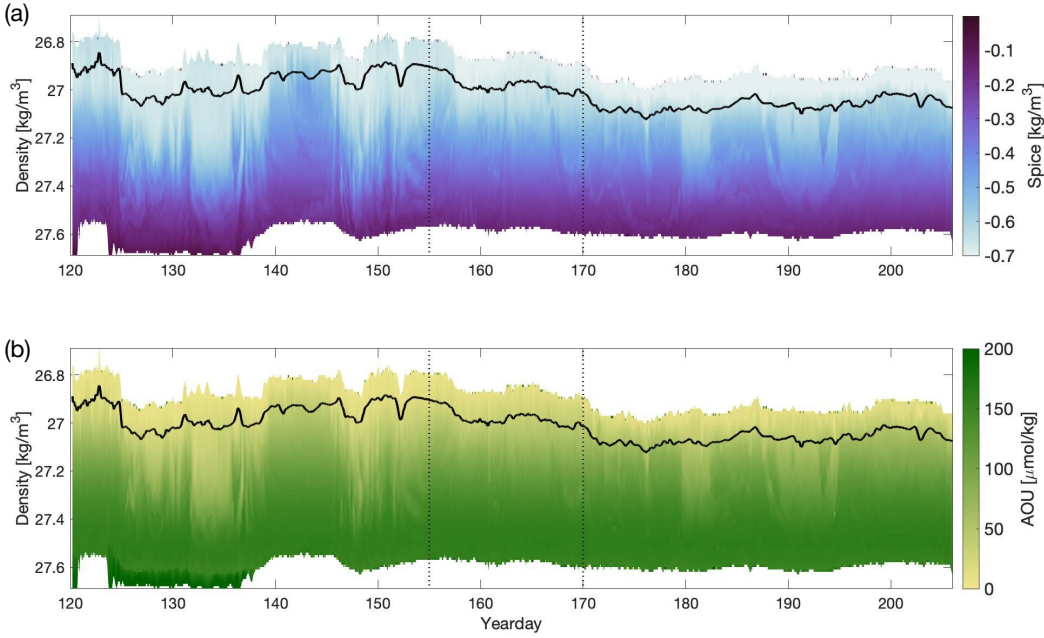


**Figure 10.** Time series of (a) spice [ $\text{kg m}^{-3}$ ] and (b) apparent oxygen utilization (AOU) [ $\mu\text{mol kg}^{-1}$ ] from glider SG660 mapped on to potential density surfaces. Black line denotes the position of the mixed layer base. Dotted line at yearday 155 denotes an end to the high-EKE region and the dotted line at yearday 170 denotes the start of the low-EKE region. Data from SG660.

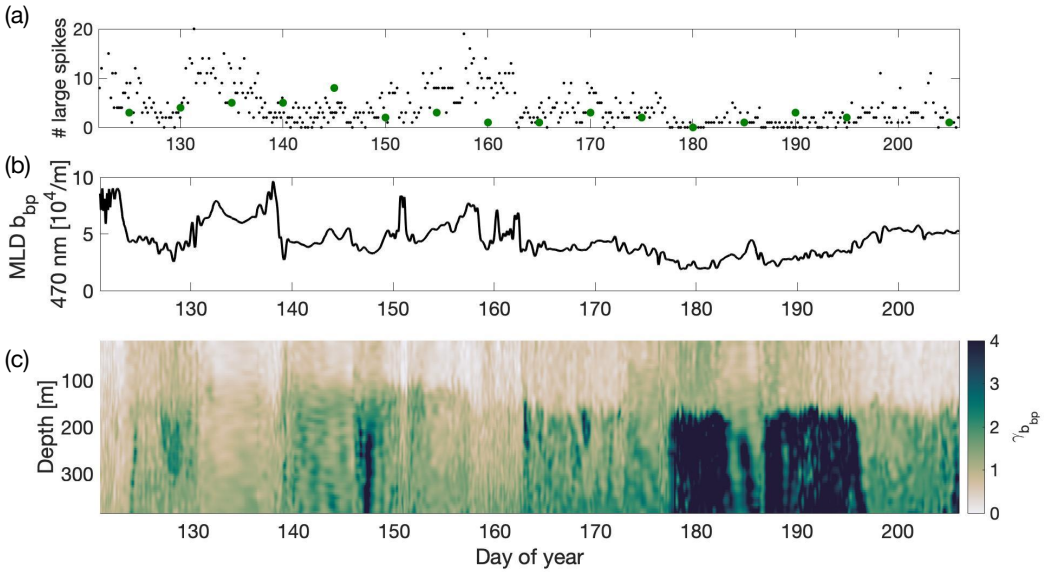


**Figure 11.** (a) Black dots: number of large spikes in 470 nm backscatter below the mixed layer per each downcast and upcast of SG659. Green dots: number of large spikes in 700 nm backscatter in BGC-Argo float data from WMO 5906030. Note that only qualitative patterns should be considered as the sampling rates of the gliders and float were not the same. (b) 470 nm backscatter in the mixed layer from SG659. (c) Backscatter spectral slope ( $\gamma_{b_{bp}}$ ) from SG659. Figure made with SG659 due to potential errors in the 700 nm backscatter data from SG660.

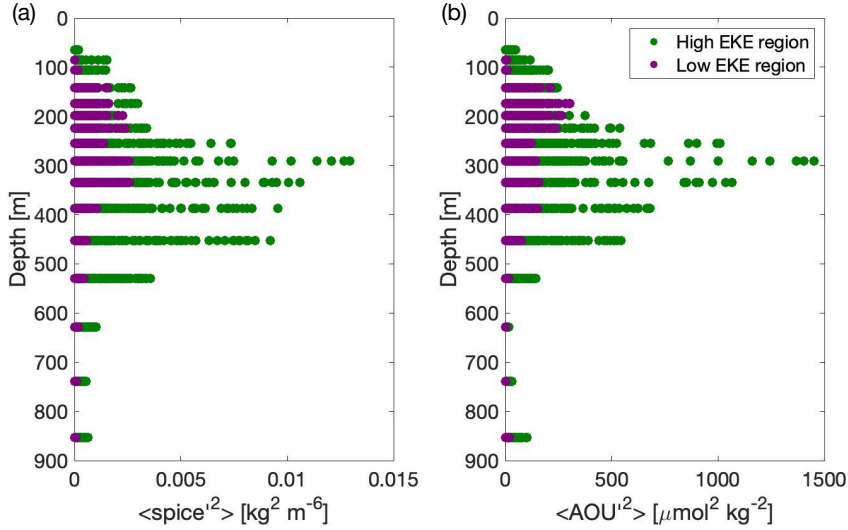


**Figure 12.** (a) Squared anomalies of spice in the high-EKE (green) and low-EKE (purple) regions on isopycnals, plotted on the average depth of each isopycnal. (b) Same as in (a) but for AOU. Individual points are the squared difference of spice (or AOU) at a point and the running mean (50 km) of spice (or AOU) along the isopycnal. Joint data of SG659 and SG660.

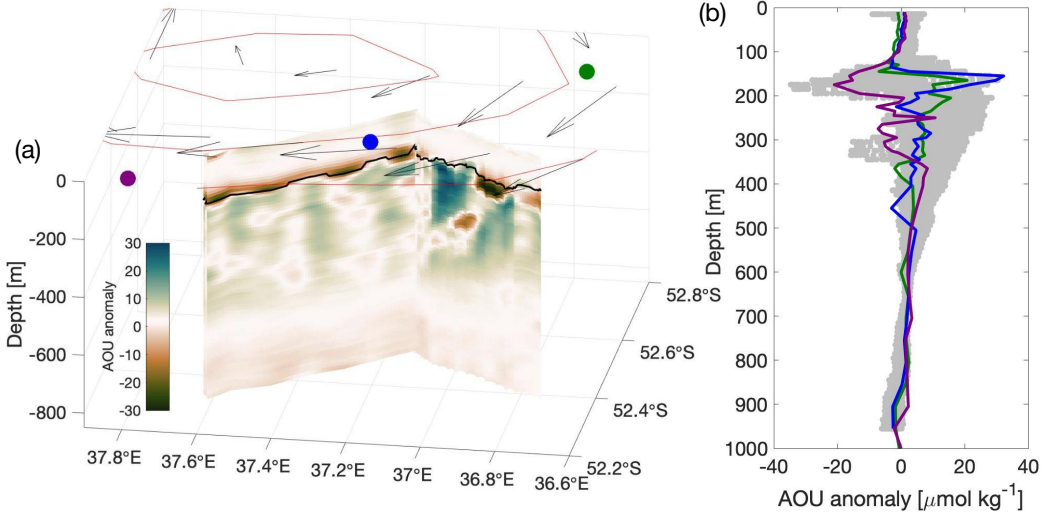


**Figure 13.** AOU anomalies in glider and float data in a mesoscale eddy. (a) Curtain figure of the AOU anomaly from the mean value at each depth from SG660 between yeardays 187-193. MLD is plotted as a black line. Sea level anomaly from day 190 is given by the red contours; the arrows show the geostrophic velocity with peak speed of ( $20 \text{ cm s}^{-1}$ ). Green, blue, and purple lines represent the locations of vertical profiles done by the BGC-Argo float on yeardays 185, 190, and 195, respectively. (b) AOU anomaly with depth for the glider (gray) and each of the 3 float profiles with the same colors as in panel (a). Note the float did every other profile to 2000 m but only the upper 1000 m are shown.

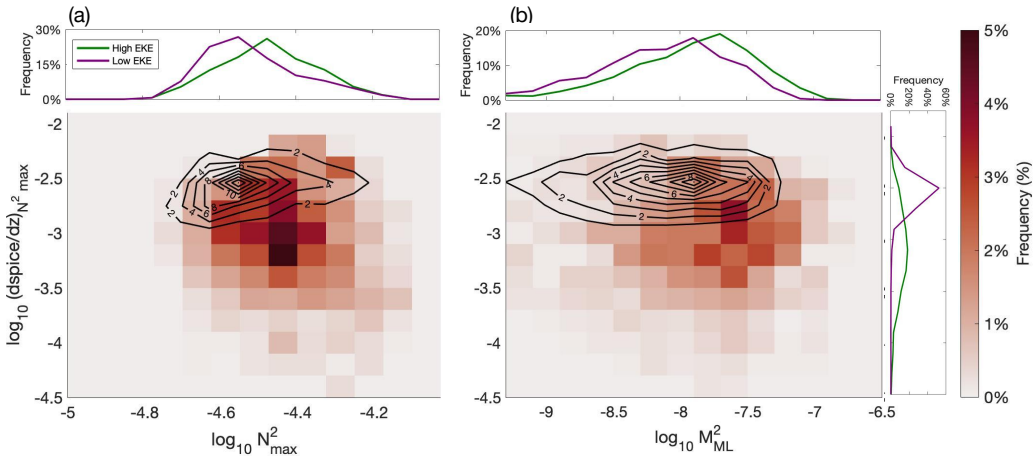


**Figure 14.** Joint probability distribution functions of (a)  $\log_{10}$  maximum vertical gradient of buoyancy ( $N_{max}^2$ ), and (b)  $\log_{10}$  horizontal gradient of buoyancy in the mixed layer ( $M_{ML}^2$ ) and with the  $\log_{10}$  of the absolute value of vertical spice gradient at the depth of  $N_{max}^2$ . Colors show the distribution for the high-EKE region; contours give that for the low-EKE region. Values of the joint probability for the contours for the low-EKE region are labeled. The one-dimensional histograms show the the probability distribution of (a)  $\log_{10} N_{max}^2$  and (b)  $\log_{10} M_{ML}^2$  for the high-EKE region (green) and low-EKE region (purple). Made from the joint data of SG659 and SG660. Discretization:  $\Delta N^2 = 0.075$ ,  $\Delta M^2 = 0.2$ ,  $dspice/dz = 0.2$ .

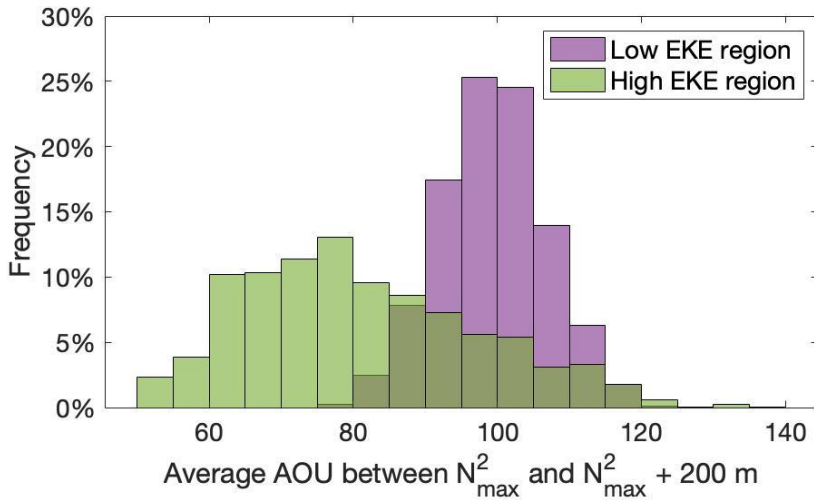


**Figure 15.** Probability distribution of the average value of AOU [ $\mu\text{mol kg}^{-1}$ ] between the depth of  $N_{max}^2$  and the depth of  $N_{max}^2 + 200\text{m}$ . Green bars represent the high-EKE region and purple bars the low-EKE region. Made from the joint data of SG659 and SG660.